Structural determinants of broadly neutralizing human antibodies binding to morphological dengue virus variants.

Ananya Chatterjee[1†], Ankush Roy[1†], Srividhya Srinivasan[1†], Sylvia Charles[1π], Jay Lubow[3Ψ], Leslie Goo[3τ] and Vidya Mangala Prasad[1,2*]

† equal contribution

Affiliations:

1. Molecular Biophysics Unit, Indian Institute of Science, Karnataka 560012, India.

2. Centre for Infectious Diseases Research, Indian Institute of Science, Karnataka 560012, India.

3. Vaccine and Infectious Disease Division, Fred Hutchinson Cancer Center, Seattle 98109, Washington, USA.

[π]Present address: Department of Chemical Engineering, University of Bath, Bath, UK.

[Ψ] Present address: ImmunoVec, 570 Westwood Plaza Building 114 ,90095, Los Angeles, California, USA.

[τ] Present address: Vaccine Company Inc., South San Francisco, California, USA.

19 *Correspondence to: vmprasad@iisc.ac.in

20

21

22 **Abstract:**

23 Dengue virus (DENV) is a global disease threat with tropical regions bearing the bulk
24 of disease burden. Presence of four DENV serotypes with varying antigenicity has
25 complicated development of effective, pan-serotype strategies for prevention and
26 treatment of dengue disease. Here, we report single-particle cryo-electron microscopy
27 (cryo-EM) structures of DENV in complex with three human-derived broadly
28 neutralizing antibodies (bnAbs), revealing an antibody class which preferentially uses
29 its heavy chain for potency and antigen recognition. These heavy chain-driven E-dimer
30 recognizing (HEDR) bnAbs potently neutralize all DENV serotypes by binding to a
31 quaternary epitope encompassing the critical fusion loop and conserved glycans on
32 DENV's surface E-glycoprotein dimer. We also demonstrate the presence of capsule-
33 shaped DENV, with HEDR antibodies binding such tubular morphologies in addition
34 to spherical virions. Cryo-EM helical reconstructions of Fab-bound tubular virions from
35 different DENV strains establishes that the pattern of E-glycoprotein's helical
36 arrangement is dependent solely on the virus strain. The structural data also
37 demonstrate that binding of highly potent HEDR bnAb D14.F25.S02 causes distortion
38 of DENV particles. Collectively, these results elucidate key features of HEDR bnAbs
39 while illustrating the importance of eliciting immune responses that can neutralize
40 diverse DENV morphologies.

41

42 **Introduction:**

43 DENV is an enveloped RNA virus which affects nearly 400 million individuals
44 worldwide giving rise to diverse clinical outcomes, including asymptomatic dengue
45 fever, joint pain, rashes, dengue shock syndrome and severe dengue haemorrhagic
46 fever[1]. The canonical mature and infectious DENV is an icosahedral particle, 500 Å in
47 diameter, with its outer membrane surface coated by its main antigenic protein, the
48 envelope (E) glycoprotein (Fig.1a,b). Each E-protein monomer (~50kDa molecular
49 weight) consists of three domains—DI, DII, and DIII—with N-linked glycosylation at
50 Asn67 and Asn153 amino acid residues[2,3] (Fig.1c). The E-protein's DII domain
51 contains the highly conserved fusion loop (~14 amino acids long) at its distal end,
52 which is crucial for viral membrane fusion within host cells during infection[3–5] (Fig.1c).
53 On the mature virion surface, the E-proteins are arranged into 90 head-tail
54 homodimers with three such E-dimers forming an E-raft that comprises two
55 asymmetric units of the virus's icosahedral surface arrangement[2] (Fig.1b,c). Despite
56 global icosahedral symmetry, the local environment for each of the E-proteins in the
57 asymmetric unit is different, and consequently, the local environment experienced by
58 the E-proteins are distinct at the icosahedral 5-fold (5f), 3-fold (3f) and 2-fold (2f)
59 symmetry positions[2] (Fig.1b,c).

60 DENV presents almost identical surface epitopes across its four serotypes [6–8],
61 giving rise to cross-reactive antibodies that are, often, poorly-neutralizing against
62 heterologous DENV strains[9,10]. Secondary infections of DENV can, thus, cause severe
63 disease due to antibody-dependent enhancement (ADE) of viral infection [11,12]. There
64 are few reported examples of broadly neutralizing antibodies (bnAbs) that neutralize
65 all DENV serotypes[10–12]. All these bnAbs bind on or near the conserved fusion loop
66 region of DENV's E-protein, highlighting the significance of this region as an

67 immunogenic target. Notably, largest breadth in neutralization activity across DENV
68 serotypes has been observed in antibodies that recognize a combination of the fusion
69 loop along with adjacent regions on a E-protein dimer[13–21]. From previously reported
70 literature, few of the best characterized bnAbs which bind a quaternary epitope
71 comprising the fusion loop and adjacent regions on the DENV E-protein are the E-
72 dimer epitope (EDE) bnAbs, which are further sub-classified as EDE1 and EDE2
73 bnAbs[19,20]. EDE1 bnAbs strongly neutralize both DENV and Zika viruses with bnAb
74 binding being independent of N153 glycosylation on DENV E-protein. In contrast, the
75 EDE2 bnAbs potently neutralize DENV, with lower activity against ZIKV, and require
76 interaction with E-protein's N153 glycan.

77 DENV populations in nature are a mixture of its mature and immature forms,
78 including virions that are partially mature to various proportions[6,22,23]. The mature and
79 immature DENV structures are markedly different, with the mature DENV surface
80 displaying 90 non-covalently bound, antiparallel E-dimers along with buried membrane
81 (M) proteins on its surface, whereas the immature DENV displays 60 trimeric spikes
82 of E-protein and precursor membrane (prM) protein heterodimers. Thus, incomplete
83 virus maturation adds a layer of structural heterogeneity to circulating DENV
84 populations. Additionally, in the past decade, DENV virions have been reported to
85 deviate from their icosahedral structures to exhibit other morphologies such as the
86 expanded/bumpy virus[24,25] and club-shaped tubular virions[26] at temperatures of 37° C
87 and above. These heterogeneities in DENV structural forms exhibit variable
88 proportions of distinct quaternary surface arrangements that are not yet fully
89 understood, with little data available on the ability of bnAbs to recognize these various
90 morphologies.

91 We describe here, cryo-EM structures of three potent, broadly neutralizing
92 human antibodies, J9, D14.F25.S02 and D14.F05.S03, in complex with the complete,
93 infectious DENV virion. All three bnAbs were isolated from patients that recovered
94 from secondary DENV infection[16,18]. J9 and D14.F05.S03 neutralize only DENV
95 whereas D14.F25.S02 neutralizes DENV as well as its relative, Zika virus (ZIKV).
96 These select bnAbs show strong neutralization activity against DENV which is
97 comparable, and in some instances, better than other known bnAbs[16,18]. The
98 structures described here demonstrate that these bnAbs form a unique class of potent
99 antibodies that bind to the quaternary E-dimer epitope encompassing the fusion loop
100 and adjacent regions of the E-proteins, with distinct features that differentiate these
101 from previously described bnAbs. We also report helical cryo-EM structures of tubular
102 DENV morphologies bound to these bnAbs, showing the capability of these bnAbs to
103 bind variant DENV morphologies. Furthermore, using different DENV strains, we
104 demonstrate that E-protein arrangement on the helical DENV-bnAb structures is
105 dictated by the virus strain and not the bound antibody.

106

107 **Results:**

108 **Cryo-EM structures of spherical DENV particles bound to bnAbs J9,**
109 **D14.F25.S02 and D14.F05.S03:**

110 In this study, we have used two DENV-2 serotype strains from different geographical
111 origins: THSTI/TRC/01 (India) and US/BID-V594/2006 (Puerto Rico). Both these
112 strains have been isolated from humans, and the respective E-glycoproteins share
113 98% identity (99% similarity) between each other and ~98% identity (~99.6%

114 similarity) with the E-protein of well-studied DENV-2/16881 strain (Supplementary Fig.
115 1). Using these strains, cryo-EM structures of spherical DENV complexed with Fabs
116 from three potent bnAbs, namely, J9, D14.F25.S02 and D14.F05.S03 were calculated
117 with icosahedral symmetry applied (Supplementary Fig.2-4). The icosahedral cryo-EM
118 structures of the DENV+J9 Fab, DENV+ D14.F25.S02 Fab and DENV+D14.F05.S03
119 Fab were determined to highest global resolutions of 3.85 Å, 4.1 Å and 4.5 Å
120 respectively (Fig1c-e, Supplementary Fig.5 and Supplementary Table 1-3). Local
121 resolution of the cryo-EM density maps, calculated from the viral membrane outwards,
122 ranges between 2.4 Å to 6.4 Å for DENV+J9 Fab complex, 2.5 Å to 7.5 Å for
123 DENV+D14.F25.S02 Fab complex, and 3.5 Å to 7.0 Å for DENV+D14.F05.S03 Fab
124 complex respectively (Supplementary Fig.5). Localised reconstruction of sub-
125 icosahedral symmetry-related positions further improved local map features and
126 glycan densities for both the DENV+J9 as well as DENV+D14.F05.S03 complex maps
127 (Supplementary Fig.6, 7).

128 In the above described cryo-EM maps of icosahedral DENV complexes,
129 densities for the E and M glycoproteins as well as the antibody-virus interface were
130 well-resolved with amino acid side-chains distinguishable in most regions of the virus
131 surface, permitting real-space refinement of atomic models of DENV E-protein and the
132 respective Fab variable regions (Fig.2a,d,g, Supplementary Fig.8, Supplementary
133 Tables 1-3). Though one Fab (~50kDa molecular weight) can bind to each E-protein
134 for all three bnAbs, none of the bnAbs show full occupancy of all the possible 180 E-
135 protein binding sites on the DENV virion, with each bnAb showing a different pattern
136 of binding across the virion (Fig.1d-i) suggesting that complete occupancy of all
137 available epitopes may not be necessary for neutralization activity of these bnAbs.

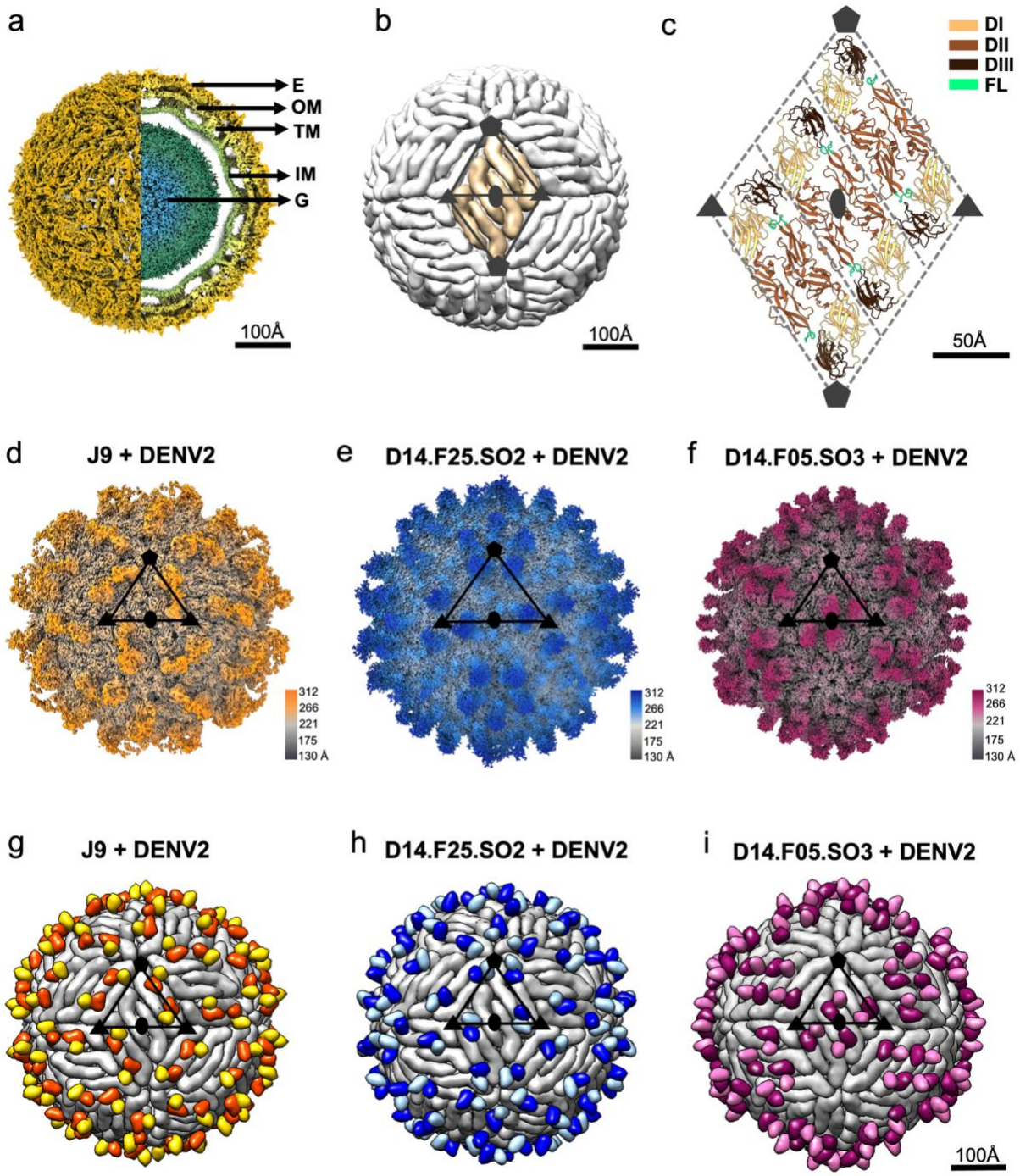

Figure 1. Cryo-EM structures of HEDR bnAbs complexed with DENV.

a. Surface and cross-sectional view of dengue virus with black arrows indicating the different virus parts: E (envelope glycoprotein layer), OM (Outer lipid membrane), TM (Transmembrane space), IM (inner lipid membrane) and G (genome core).

143 **b.** Surface representation of DENV virion showing icosahedral arrangement of E-
144 proteins in grey. Black triangles indicate the icosahedral asymmetric unit. A single
145 E- raft comprising of three E-dimers is coloured in beige and marked by a rhombus.
146 Each asymmetric unit repeats itself 60 times to form the spherical virus surface.
147 Despite the global icosahedral symmetry, the local environment around each E-
148 protein in the asymmetric unit is distinct and consequently, the local environment
149 experienced by the E-proteins at the 5-fold, 3-fold and 2-fold vertices are different,
150 which introduces an element of non-symmetry in virus-antibody interactions at
151 these vertices.

152 **c.** Cartoon representation of an E-dimer raft, also referred to as an E-raft, consisting
153 of three adjacent E-dimers. Parts of the E-protein are colored as: Domain-1 (DI) in
154 mustard yellow, Domain-2 (DII) in brown with the fusion loop (FL) in green and
155 Domain-3 (DIII) in black.

156 **d-f.** Radially coloured, high-resolution cryo-EM reconstructions of DENV complexed
157 with J9 (d), D14.F25.S02 (e) and D14.F05.S03 (f) Fab fragments.

158 **g-i**. Surface model representation of the cryo-EM reconstructions shown in d-f panels.
159 The E-proteins are colored as grey surface similar to panel b, The variable region of
160 the Fab fragments is represented also as surface models. **g.** DENV complexed with
161 J9 Fab (Orange- heavy chain, Yellow- light chain). **h**. DENV complexed with D14.F25.S02
162 Fab (Dark blue- heavy chain, Light blue- light chain). **i.** DENV complexed with
163 D14.F05.S03 fab (Dark pink- heavy chain, Light pink- light chain).

164 In all panels, the 5-fold, 3-fold and 2-fold icosahedral symmetry vertices are indicated
165 by a hexagon, triangle and ellipse, respectively.

166

167 **Epitope features of bnAbs J9, D14.F25.S02 and D14.F05.S03 on icosahedral**
168 **DENV:**

169 All three bnAbs bind to the fusion loop region and interact with the N153 glycan,
170 with the Fab footprints covering parts of DI and DIII domains from the adjacent E-
171 protein in an E-dimer (Fig.2, Fig.3a and Supplementary Fig.9, 10). The bnAbs require
172 interactions that span the E-dimer surface (Fig.2b,e,h, Fig.3a, Supplementary Tables
173 4-6), which explains why these were previously reported as not binding E-monomers
174 in solution[16,18]. All three bnAbs show overlapping epitope footprints, despite
175 differences in their angle of approach to the E-protein (Fig.3, Supplementary Fig.10).
176 All three bnAbs bind to the E-protein's fusion loop using its heavy chain CDR3
177 (HCDR3) loop (Fig.2a,d,g, Fig.3 a,b and Supplementary Figure 9). The tip of J9's
178 HCDR3 is positioned towards the intra-E-dimer cleft, whereas the D14.F05.S03's
179 HCDR3 loop is positioned on top of the fusion loop (Fig.3b). Notably, in D14.F25.S02,
180 its HCDR3 loop interacts in a sideway fashion with the E-protein's fusion loop, such
181 that the HCDR3 is inserted within the inter-dimer space between adjacent E-dimers
182 (Fig.3b). Furthermore, the HDCR3 from all three bnAbs also make contacts with the
183 conserved N153 glycan on E-protein (Fig.2c,f,i).

184 The overall epitope footprint of the three bnAbs (Fig.2b,e,h and Fig.3a) overlaps
185 broadly with previously described EDE bnAbs[20]. However, the clusters of E-protein
186 amino acid residues that are critical for bnAb binding and neutralization, as determined
187 from these structural data and corroborating functional assays[16,18], are distinct
188 between the different bnAbs, indicating local variations in binding determinants
189 (Supplementary Fig.9). Furthermore, all three bnAbs make majority of interactions with

190 the DENV E-protein using its heavy chain (Supplementary Tables 4-7), with the bnAb
191 heavy chain involved in interactions with both the fusion loop (Fig.2a,d,g and 3b) and
192 conserved N153 glycan (Fig.2c,f,i), grouping them as a separate class of their own,
193 hereon referred to as heavy chain-driven E-dimer recognizing (HEDR) antibodies.

194

195 **Interactions with E-protein glycans by the HEDR bnAbs, J9, D14.F25.S02 and**
196 **D14.F05.S03:**

197 The HEDR bnAbs can be classified into two categories, similar to the EDE
198 bnAbs[19,20], based on their dependence on E-protein's N153 glycan for neutralization
199 activity. D14.F25.S02 forms HEDR category-1 which is independent of N153
200 glycosylation for its neutralization activity. Nevertheless, D14.F25.S02 bnAb makes
201 multiple contacts with the N153 glycan (Fig2f, Supplementary Table 5), in contrast to
202 the previously described EDE1 bnAbs which induce disordering of the N150 loop
203 containing the N153 glycan[15,20]. In further contrast to EDE1 bnAbs[20], HEDR category-
204 1 bnAb, D14.F25.S02, does not show any interactions with the E-protein's N67 glycan
205 (Fig. 2f). On the other hand, HEDR category-2 bnAbs include J9 and D14.F05.S03,
206 show many similarities with the EDE2 bnAbs, including the requirement of N153
207 glycosylation for its neutralization activity[16,19]. J9 and D14.F05.S03 make close
208 contacts to the N153 glycan making it an integral part of the bnAb epitope (Fig.2c,i,
209 Supplementary Table 4, 6). J9 uses its heavy chain to interact with the lower part of
210 the N153 glycan via hydrophobic and electrostatic interactions, whereas the light chain
211 contacts the terminal glycan residues via primarily electrostatic interactions (Fig.2c,
212 Supplementary Table 4). Similar pattern of engagement is seen with D14.F05.S03
213 also with the Fab heavy chain making multiple contacts to the lower part of the N153

214 glycan (Fig.2i, Supplementary Table 6). J9 and D14.F05.S03 also make close contacts
215 with the E-protein's other conserved glycan at N67 position (Fig2c,i, Supplementary
216 Tables 4, 6), though this glycan is not necessary for its neutralization activity. As the
217 spatial position of N153 glycan in DENV's E-protein is different with respect to the
218 equivalent N154 glycan position in ZIKV's E-protein, the structural data suggests that
219 close interactions with N153 glycan may influence differential recognition of DENV by
220 the HEDR category-2 bnAbs, J9 and D14.F05.S03.

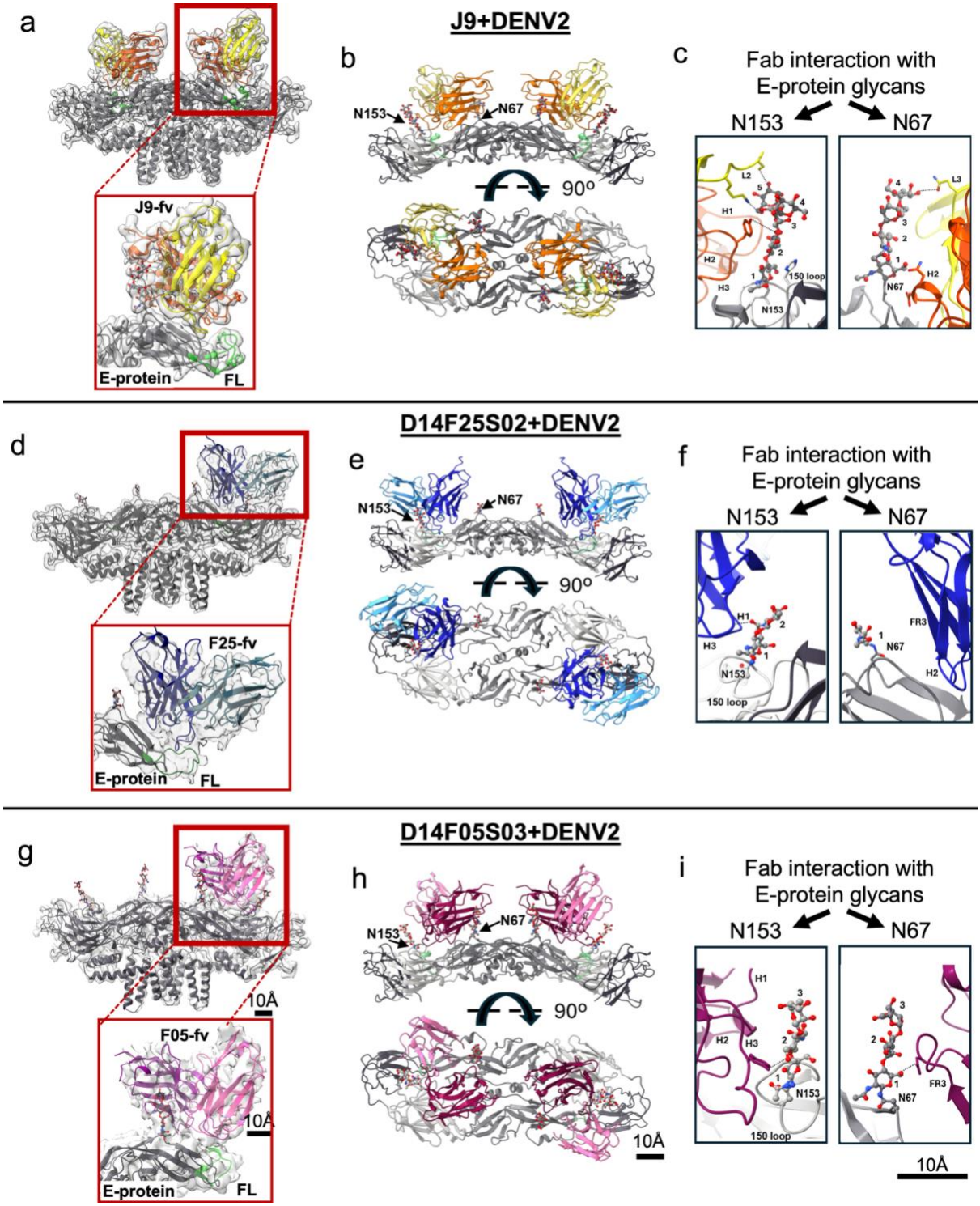

221

222 **Figure 2. Quaternary binding epitopes of HEDR bnAbs on DENV E-dimer.**

223 **a,d,g.** Density map cutouts of DENV E-dimer and Fab complexes from the

224 icosahedral cryo-EM structures shown in Figure 1d-f. The maps cutouts also include

225 the built-in atomic models for each of the complexes (DENV-E+M protein and Fab

226 variable regions) showing the accuracy of the protein models. In all panels of this

227 figure, the E-dimer ribbon models are shown in dark grey. The ribbon models of each
228 Fab variable region (Fv) are also shown, with J9 Fv colored in orange (heavy chain)
229 and yellow (light chain), D14.F25.S02 colored in dark blue (heavy chain) and cyan
230 (light chain), D14.F05.S03 colored in dark pink (heavy chain) and light pink (light
231 chain) and fusion loop region in green.

232 **b,e,h.** Top and side view of atomic models of E-dimer ectodomain complexed with
233 Fab variable regions of J9 (b), D14.F25.S02 (c) and D14.F05.S03 (e) respectively. In
234 all three atomic model representations, the glycan positions are marked as N153 and
235 N67.

236 **c,f,i**. Interactions of bnAbs J9 (h), D14.F25.S02 (i) and D14.F05.S03 (j) with
237 conserved glycans, N153 (left) and N67 (right) on E-protein. Black dotted lines
238 indicate the closest interacting residues. Glycan units are numbered 1 to 5 starting
239 from the closest unit to the Asn side chain.

240

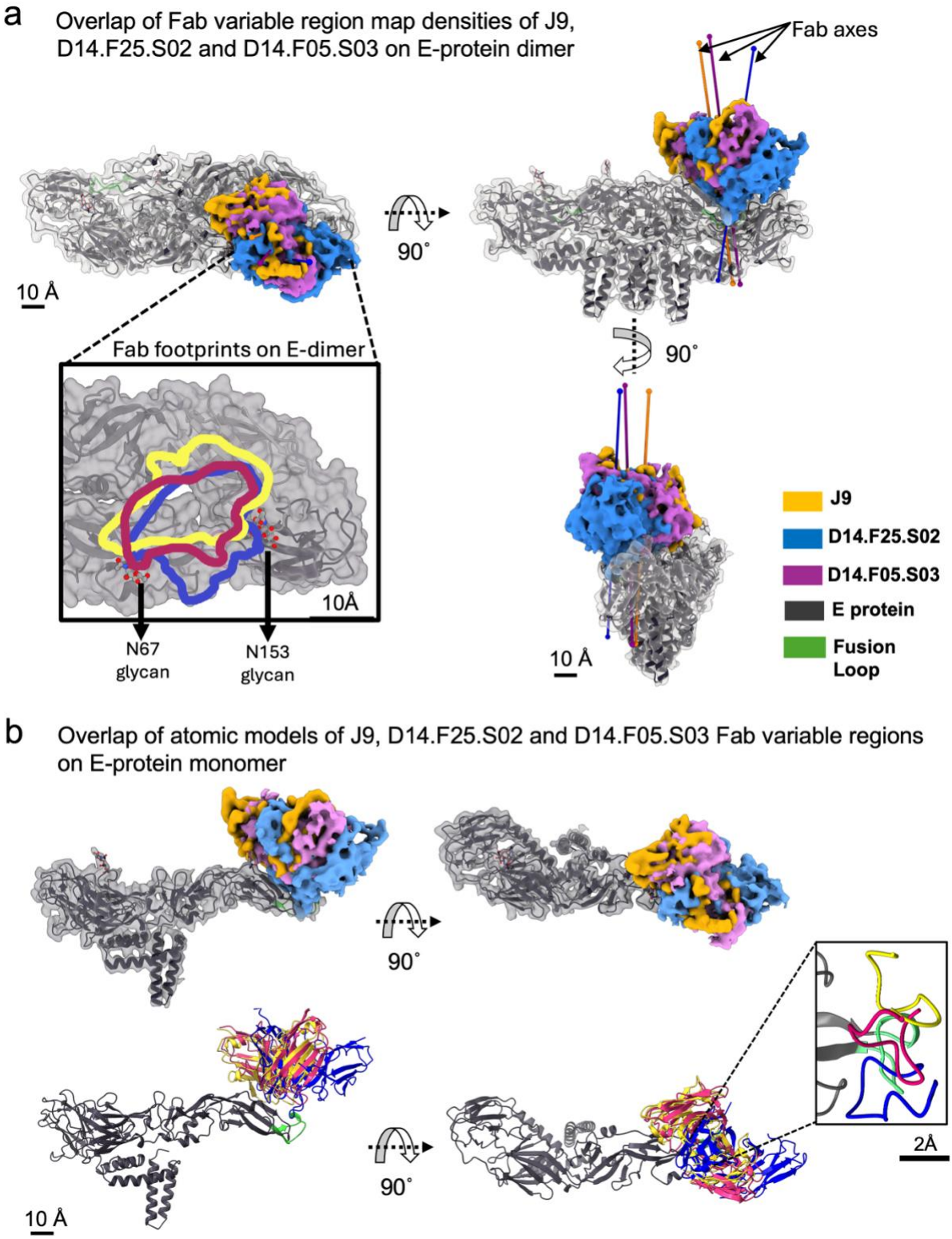

Figure 3. Overlap of bnAb binding locations and epitopes.

a. Overlapping location of the map density volumes of all three Fab variable regions (J9, D14.F25.S02 and D14.F05.S03) on E+M-dimer. Zoomed-in panel shows the top

245 view of bnAb footprints on one of the E-dimer binding positions. The bnAb footprint
246 outlines are colored as J9: yellow, D14.F25.S02: blue and D14.F05.S03: magenta.

247 **b.** Location of overlapping binding positions of all three Fabs on E-monomer. Top
248 panels show the Fabs as density volumes and E-monomer as a ribbon model built-in
249 to its electron density. Bottom panels show the Fabs and E-monomer as ribbon
250 models. Left panels show the side view and the right panels show the top view. Color
251 scheme is the same as panel a. Zoomed-in top view shows the HCDR3 loop
252 positions of J9 (yellow), D14.F25.S02 fab (blue) and D14.F05.S03 fab (magenta)
253 with respect to the E-protein's fusion loop (green).

254

255 **Morphological features of tubular and capsule-shaped DENV present in virus**
256 **preparations:**

257 Virus preparations used in this study were produced by infection of mosquito
258 cells and incubated with Fabs at room temperature without any treatment at higher
259 temperatures. Nonetheless, DENV particles with tube-like morphologies and bound
260 Fab were observed as a small percentage (<15%) in all the cryo-EM datasets collected
261 for both the US/BID-V594/2006 as well as THSTI/TRC/01 strains. Individual virions
262 were captured from both DENV strains with different lengths of tube-like extensions
263 connected to a spherical head (Supplementary Fig.13-14), reminiscent of the club-
264 shaped DENV morphology described previously[26]. Furthermore, in case of the
265 US/BID-V594/2006 strain, completely tubular virions similar to cylindrical capsules
266 were also observed (Fig.4a,b). The capsule-shaped DENV particles have similar
267 widths as the tube-like extensions observed developing from spherical virions of the

268 same strain, suggesting that capsule-shaped virions form via alterations to the
269 spherical virus (Supplementary Fig. 11). The capsule-shaped virions have an inner
270 diameter of 110 Å and 120 Å in the D14.F25.S02- and J9-bound datasets respectively,
271 with average length of particles being 79nm and 74nm respectively (Fig.4a,b). Thus,
272 the capsule-shaped virions enclose a volume large enough to contain 1.9 – 2.2 copies
273 of the viral genome (see Methods for details), indicating that these morphological
274 variants can accommodate the viral genome in its entirety.

275

276

277 **Cryo-EM structures of tubular DENV2-US/BID-V594/2006 virions bound to**
278 **D14.F25.S02 and J9 Fab fragments:**

279 Cryo-EM reconstruction of the tubular regions of DENV2-US/BID-
280 V594/2006+D14.F25.S02 Fab complex using helical symmetry parameters achieved
281 a global resolution of 14.7 Å (Fig.4c; Supplementary Fig.11a-f, 12a). In this structure,
282 E-dimers are arranged one next to another with a gentle rise, wrapping tightly around
283 the membrane tube (Fig.4c-e, Supplementary Fig.11 a-e), with two Fabs bound per E-
284 dimer, in similar positions as in the icosahedral structures. Overlapping three adjacent
285 E-dimer atomic models from the helical structure with the icosahedral E-raft structure
286 shows good agreement with an r.m.s.d value of 1.04 Å, confirming that the E-raft
287 contacts seen in spherical virions are preserved in the helical structure of DENV2-
288 US/BID-V594/2006+D14.F25.S02 Fab complex (Fig.4e,f). This helical arrangement of
289 E-proteins resembles the E-protein arrangement previously reported in the helical
290 structure of ZIKV, a close relative of DENV, complexed with an EDE1 antibody[26].

291 Similar helical patterns were observed in the J9+US/BID-V594/2006 dataset also, but
292 only a very low resolution helical cryo-EM reconstruction was determined due to few
293 tubular particle numbers (Fig.4g; Supplementary Fig.11g-i, 12b). Rigid body fitting of
294 the E-dimer and Fab complex model into the J9+DENV2-US/BID-V594/2006 map
295 (Fig.4h, Supplementary Fig. 11i) showed that the E-dimer arrangement is similar to
296 that observed with the D14.F25.S02+DENV2-US/BID-V594/2006 helical
297 reconstruction (Fig.4e), albeit with a rotation of 26º along an axis perpendicular to the
298 plane of the E-dimer.

299

300

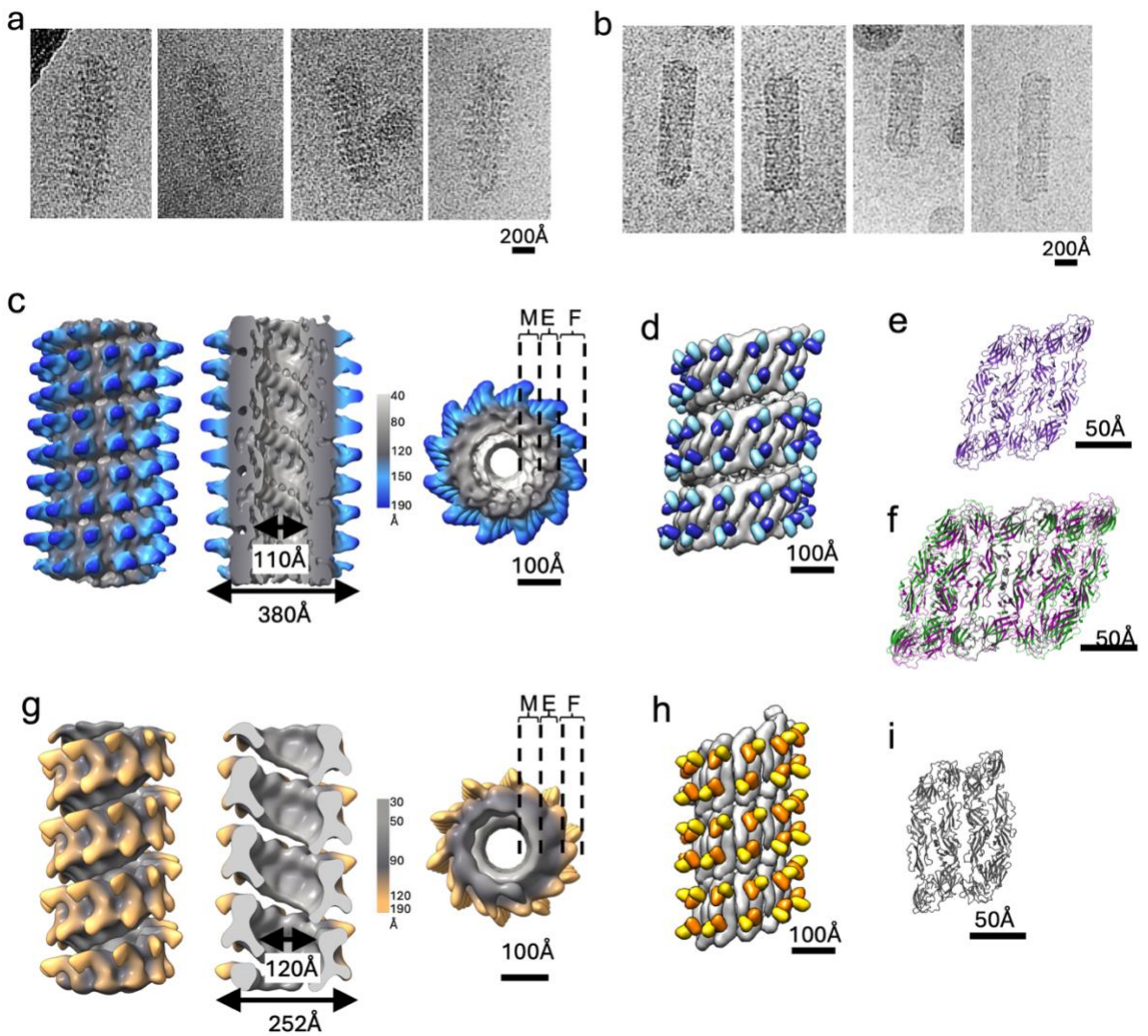

Figure 4. Capsule-shaped DENV show helical symmetry arrangement in Fab-bound state.

a-b. Representative raw cryo-EM images of capsule-shaped DENV2-US/BID-V594/2006 virions bound with D14.F25-S02 Fab (a) and J9 Fab (b). Spiky Fab projections perpendicular to the smooth virus surface is observed with presence of ordered arrangement of proteins visible.

c. Map representation of surface (left) and longitudinal cut-out (centre) and top view (right) of the helical reconstruction of D14.F25.S02 Fab complexed with DENV2-

310 US/BID-V594/2006. M, E and F represent the membrane, E-protein and Fab density
311 regions, respectively, in the density map.

312 **d**. Surface representation of fitted models of the E-dimer and D14.F25.S02 Fab
313 variable region into the Fab-bound DENV2-US/BID-V594/2006 helical structure.

314 **e.** Ribbon diagram of adjacent E-dimer positions in the D14.F25.S02 + DENV2-
315 US/BID-V594/2006 helical structure.

316 **f.** Overlap of three adjacent E-dimer atomic models from the D14.F25.S02 + DENV2-
317 US/BID-V594/2006 helical structure (purple) to an E-raft from the DENV2-US/BID-
318 V594/2006 icosahedral structure (green), showing similarity in E-dimer arrangement
319 and an r.m.s.d value of 1.04Å.

320 **g.** Map representation of surface (left) and longitudinal cut-out (centre) and top view
321 (right) of the helical reconstruction of J9 Fab complexed with DENV2-US/BID-
322 V594/2006. M, E and F represent the membrane, E-protein and Fab density regions,
323 respectively, in the density map.

324 **h.** Surface representation of fitted of the E-dimer and J9 Fab variable region into the
325 Fab-bound DENV2-US/BID-V594/2006 helical structure.

326 **i.** Ribbon diagram of adjacent E-dimer positions in the J9 + DENV2-US/BID-
327 V594/2006 helical structure. This E-dimer arrangement is similar to that seen in the
328 D14.F25.S02+DENV2-US/BID-V594/2006 helical structure after rotation of 26º along
329 an axis perpendicular to the plane of the E-dimer. R.m.s.d between the two E-dimer
330 arrangements in panel e and i (after superposition with rotation) is 0.875Å.

331

332 **Cryo-EM structures of tubular DENV2-THSTI/TRC/01 virions bound to J9,**
333 **D14.F05.S03 and D14.F25.S02 Fab fragments:**

334 For the DENV2-THSTI/TRC/01 strain, Fab-bound particles with a spherical
335 head and narrow tube-like extension were observed (Supplementary Fig.13b,f, 14a).
336 These tubular extensions were selected and subjected to unsupervised 2D
337 classification, which also showed clear helical patterns (Supplementary Fig.13b,g
338 14b). Helical cryo-EM reconstructions of THSTI/TRC/01 virions were achieved to
339 global resolutions of 14.41Å for J9-bound, 17.3Å for D14.F05.S03-bound and 17.37 Å
340 for the D14.F25.S02-bound particles respectively (Fig.5, Supplementary Fig. 13, 14,
341 15). The outer and inner diameters of THSTI/TRC/01 tubular particles were 312 Å and
342 20 Å for the J9-virus complex, 280 Å and 55 Å for D14.F05.S03-virus complex, and
343 320 Å and 20 Å for the D14.F25.S02-virus complex respectively (Fig.5). The narrow
344 inner diameters of the tubes in the THSTI/TRC/01 strains cannot accommodate the
345 viral genome, indicating that the viral RNA is contained in the spherical head regions
346 only. The narrow inner tube diameter could, thus, restrict these virions from
347 transitioning to complete cylinders or capsule-shaped particles.

348 Despite the differences in tube diameters observed in all three helical
349 THSTI/TRC/01 structures, the E-dimers adopt a similar steep step-like arrangement
350 of E-dimer around the membrane tube (Fig.5), which differs remarkably from the E-
351 dimer arrangement observed in the helical US/BID-V594/2006 structures (Fig.3). In
352 both the J9- and D14.F05.S03-bound helical structures from THSTI/TRC/01, two Fabs
353 are bound per E-dimer with the external tips of the Fab densities joined to each other.
354 Rigid body fitting of the Fab atomic models into the map density indicates that the

355 constant regions of the Fabs would clash with each other in this conformation (Fig.5a,b,
356 Supplementary Figs. 13d,e, 14e-g). However, no such clashes were observed in the
357 respective icosahedral structural models (Fig.1d,f, Supplementary Fig. 13e,14g). In
358 spherical DENV virions, the E-protein conformation has a slight curve to match the
359 curvature of the virus. Modelling the Fab structures to a flat conformation of the E-
360 proteins, generally observed in purified E-protein structures[20,27], shows clashing of Fab
361 constant domains similar to that observed in the helical structures of the DENV-
362 THSTI/TRC/01+ Fab complexes (Supplementary Fig.13d,e, 14e-g). These analyses
363 suggest that the E-dimer adopts a flatter conformation in the tubular virions when
364 compared to its spherical counterpart. In case of D14.F25.S02, only one Fab density
365 is observed per E-dimer in the DENV-THSTI/TRC/01 tubular reconstruction. Fitting the
366 atomic models of the E-dimers and D14.F25.S02 Fab variable region in the cryo-EM
367 map suggests that the close juxtaposition of the tips of adjacent E-dimers in the helical
368 structure restricts binding of a second Fab due to probable clashes (Fig.5c,
369 Supplementary Fig.13f-k).

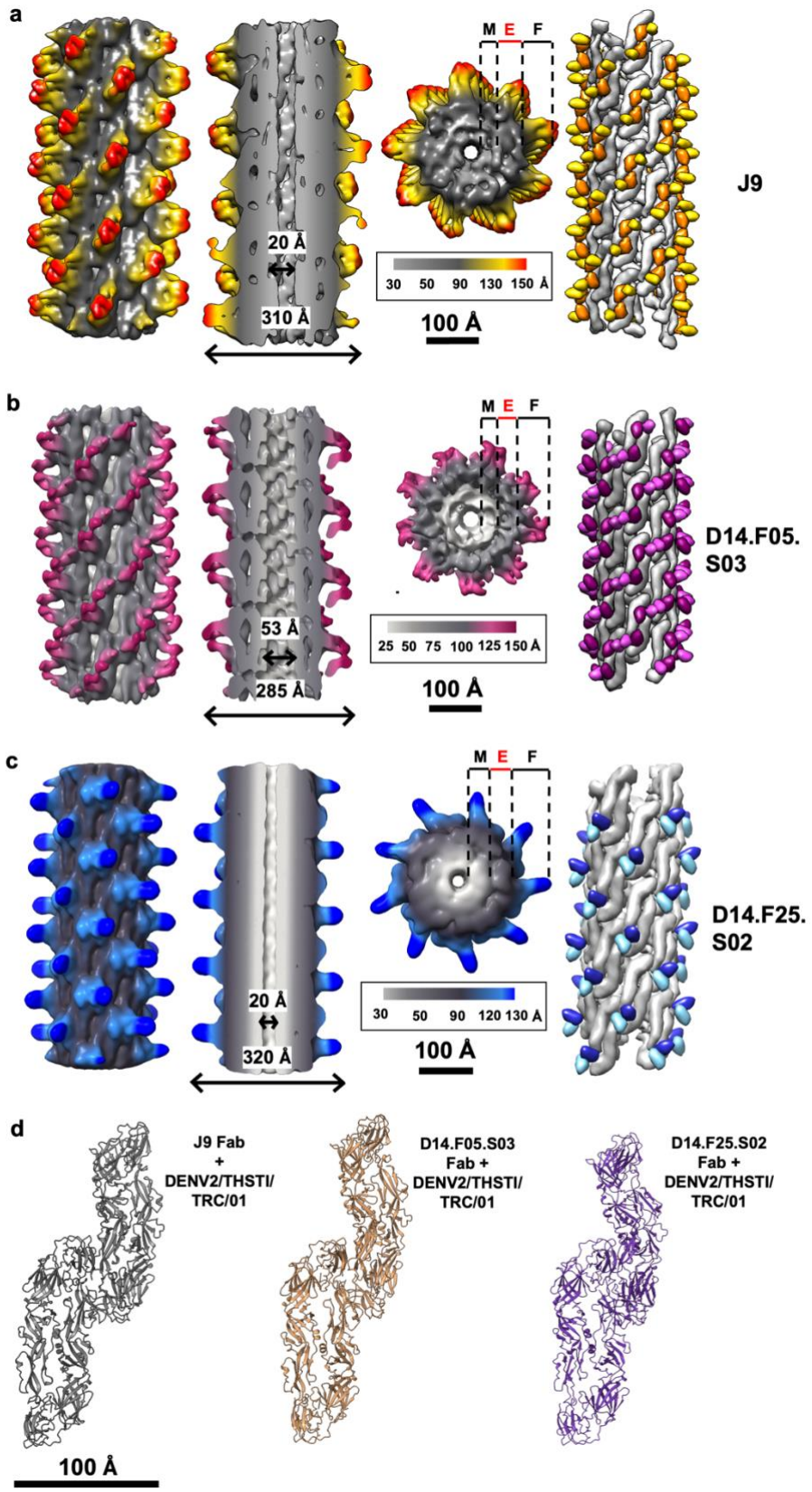

370

371 **Figure 5: Helical reconstruction of DENV2/THSTI/TRC/01 complexed with J9,**

372 **D14.F05.S03 and D14.F25.S02 Fab fragments.** Side view, central cut-out, top view

373 and surface rendered helical density map of DENV2/THSTI/TRC/01 + J9 Fab **(a)**,
374 DENV2/THSTI/TRC/01 + D14.F05.S03 Fab **(b)**, and DENV2/THSTI/TRC/01 +
375 D14.F25.S02 Fab **(c)** complexes. Each helical density map is colored based on its
376 radius from the central helical axis. In the surface rendered view (right panels of a-c),
377 only the Fab variable region is shown. (d) Comparison of adjacent E-dimer positions
378 in all three Fab-bound THSTI/TRC/01 helical structures showing similar E-dimer
379 arrangements. This similarity in adjacent E-dimer arrangement is reflected in the
380 similar helical parameters obtained for the three helical structures of
381 DENV2/THSTI/TRC/01 complexed with J9 (Rise=15.19 Å, Twist=80.62°),
382 D14.F05.S03 (Rise=15.01 Å, Twist=79.94°) and D14.F25.S02 (Rise=15.13 Å,
383 Twist=80.09°).

384

385

386 **Structural features of D14.F25.S02 Fab and IgG binding on spherical DENV and**
387 **its implications:**

388 Three-dimensional (3D) classification of spherical virions from the DENV2-US/BID-
389 V594/2006 + D14.F25.S02 Fab complex dataset resulted in two distinct classes of
390 bound virions. The 4.1Å resolution cryo-EM structure was achieved with the larger
391 class of particles which contained Fab bound to only the icosahedral 5-fold (5f) and 3-
392 fold (3f) symmetry positions with negligible density observed at the icosahedral 2-fold
393 axes (2f) (hereafter referred to as 5f-3f map) (Fig.1e). The Fab occupancy is very low
394 in the cryo-EM map, with 5f and 3f Fab occupancy estimated to be approximately 25
395 % and 18 % respectively (calculated as percentage of the average map value of

396 Fab/E-protein[28]). Moreover, though the Fab positions are similar at both 5f and 3f
397 positions, only the Fab density at 5f position was defined enough to carry out real
398 space refinement of the Fab variable chain region.

399 The smaller class contained particles where the D14.F25.S02 Fab was bound
400 only at the icosahedral 3-fold (3f) and 2-fold positions (2f) (hereafter referred to as 2f-
401 3f map) (Fig.6a). Refinement of the 2f-3f class, with icosahedral symmetry imposed,
402 resulted in a cryo-EM map of 8.45 Å global resolution (Fig5a, Supplementary
403 Fig.16a,b). The Fab occupancy in the 2f-3f map was 39%, with both 3f and 2f positions
404 bound equivalently. However, only 20% of particles formed the 2f-3f class compared
405 to the 5f-3f class, indicating that the Fab binds to the 5f position robustly. The Fab
406 footprint and angle of approach are equivalent in both 2f-3f and 5f-3f maps (Fig.1e,
407 2c, Fig.7a, Supplementary Fig. 16c). Though there is no evidence of potential clashes,
408 comparing the Fab structural models bound to symmetry-related positions on the virion
409 suggest that binding of D14.F25.S02 to 5f position affects Fab binding to the 2f
410 positions, as is seen in the negligible Fab occupancy at 2f positions in the 5f-3f map.
411 Attempts to perform localized reconstruction of the Fab-bound E-dimers at the 5f and
412 3f symmetry positions did not yield any 3D classes with better Fab densities, which
413 could be due to the low Fab occupancy. Analysis of 2D classes shows that saturation
414 level binding of D14.F25.S02 bnAb causes distortion of the spherical virions
415 (Supplementary Fig.16d). Spherical virions are only observed in 2D classes that
416 contain feeble Fab projections suggesting lower binding ratio of Fab molecules to
417 virions (Supplementary Fig.16d).

418 Cryo-EM analyses of DENV2-US/BID-V594/2006 complexed to D14.F25.S02
419 IgG was also attempted to get a broader sense of bnAb epitope binding

420 (Supplementary Fig.17a). Massive aggregation of virions was observed in the dataset
421 with few isolated virions (Supplementary Fig.17b). Single-particle cryo-EM
422 reconstruction was calculated from a small subset of non-aggregated and loosely
423 aggregated virions to a global resolution of 7.7 Å with a local resolution range of 4.5
424 to 10 Å (Fig.6b, Supplementary Fig.17a,c,d). The IgG binding positions on the virion
425 are identical to that observed with the Fab (Figure 1,2 and Supplementary Fig.16), and
426 the bnAb binding occupancy at all symmetry-related epitope sites was approximately
427 26%. 3D classification did not yield any differentially bound IgG subsets as observed
428 with the Fab-bound dataset, which could be due to the lower number of isolated
429 particles in the IgG dataset. The IgG map density could be resolved only till the Fab
430 region, and no density was observed for the Fc portion of the IgG, even at very low
431 thresholds (Supplementary Fig.17f). This observation along with massive aggregation
432 seen in the dataset suggests that the two arms of the IgG cross-link adjacent virions.
433 The overall low occupancy of Fab arms in the averaged IgG+DENV complex
434 reconstruction further reinforces that the D14.F25.S02 binding is relatively weak
435 across different epitope positions on the virus.

436 Despite several attempts, it was not possible to achieve a high resolution cryo-
437 EM structure of D14.F25.S02 Fab complexed to the DENV2-THSTI/TRC/01 strain.
438 The best possible 3D reconstructed map of D14.F25.S02 Fab+DENV2-THSTI/TRC/01
439 complex achieved a global resolution of ~19 Å showing Fabs bound equivalently at all
440 symmetry related positions in the cryo-EM map (Fig.6c). However, the Fab and E-
441 protein features lack definition, suggesting higher variability in the constituent virions
442 (Fig.6c, Supplementary Fig.18). Analysis of 2D classes from the DENV2-
443 THSTI/TRC/01+ D14.F25.S02 Fab dataset showed clear distortion of Fab-bound

444 virion particles, indicating that the virus morphology was dramatically affected by
445 D14.F25.S02 Fab binding (Supplementary Fig.18b).

446 Analysing the binding epitope of D14.F25.S02 shows that the bnAb contacts
447 span both intra-E-dimer and inter-E-dimer regions (Fig.2c, 5d,e and Supplementary
448 Fig.9). Majority of the Fab interactions within an E-dimer is carried out by the Fab
449 heavy chain through contacts to DI and DII domains, with the Fab light chain making
450 minimal contacts with DI and DIII domains (Supplementary Fig.9 and Supplementary
451 Table 5). However, the Fab light chain is solely involved in inter-E-dimer contacts
452 between adjacent E-rafts and also within an E-raft (Fig.6d,e). At the icosahedral 5f
453 position, the Fab light chain has a different local environment when compared to the
454 2f and 3f positions and makes numerous contacts to the DI and DIII domains of E-
455 proteins in adjacent E-dimer rafts (Fig. 5d, Supplemental Table 2). E-protein residues,
456 Tyr 178 and Met 297, which have been implicated in neutralization activity of
457 D14.F25.S02[16] are located within bnAb footprint at the 5f position, indicating that these
458 inter-raft contacts are essential for the bnAb activity (Fig.6d). In contrast,
459 D14.F25.S02's light chain interactions with adjacent E-dimers within an E-raft are
460 minimal (Fig.6e, Supplementary Table 5) and not necessary for its binding or
461 neutralization activity[16].

462

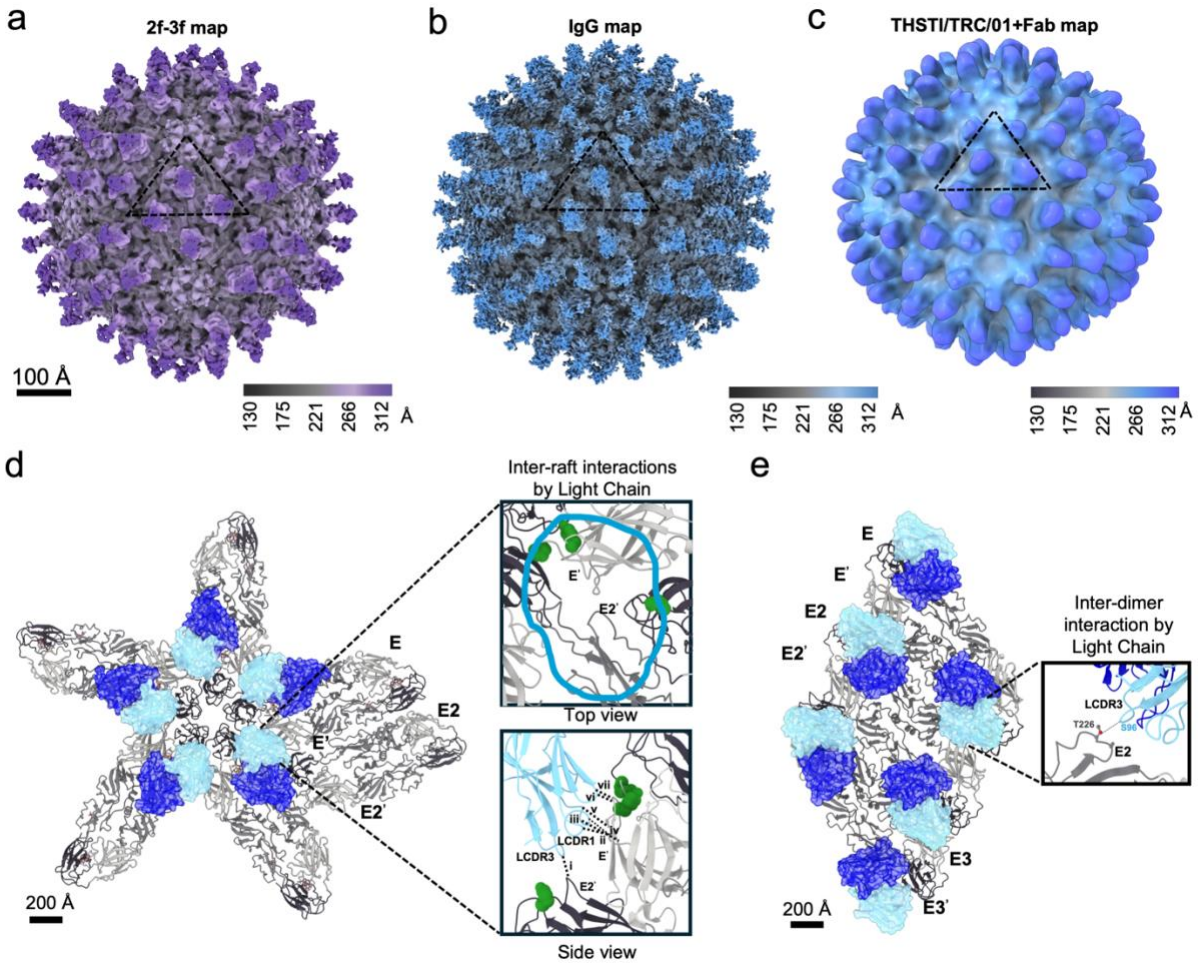

Figure 6. **Cryo-EM reconstructions of D14.F25.S02 Fab and IgG bound to DENV strains.**

a. Surface rendered 2f-3f cryo-EM density map of D14.F25.S02 Fab + DENV2-US/BID-V594/2006 complex.

b. Surface rendered cryo-EM density map of D14.F25.S02 IgG + DENV2-US/BID-V594/2006 complex.

c. Surface rendered cryo-EM density map of D14.F25.S02 Fab + DENV2-THSTI/TRC/01 complex. Panels a-c are colored radially from the centre and icosahedral asymmetric unit labelled as a dotted triangle.

473 **d**. Top view of icosahedral 5f position from D14.F25.S02 Fab + DENV2-US/BID-
474 V594/2006 complex showing inter-E-raft interactions made by D14.F25.S02 light
475 chain. E-proteins are shown as ribbons and Fabs are shown as surface
476 representations. Zoomed-in panels show top view and side view of inter-E-raft
477 interaction regions. Amino acid residues important for neutralization have been
478 depicted as green-colored balls. In the zoomed-in top view, cyan outline indicates the
479 Fab footprint. In the side-view, contacts between the Fab light chain and E-protein
480 residues have been labelled as dotted lines, (i) S96->P384 (ii) S26->E174 (iii) G31->
481 E174 (iv) G30-> E174 (v) K33-> G179 (vi) S69-> T176 (vii) G70->T176 respectively.
482 Residue contacts are calculated as residues with <8Å distance between Cα-Cα
483 backbone of Fab and E-protein respectively.

484 **e**. Top view of inter-E-dimer interactions within an E-raft from the D14.F25.S02 Fab +
485 DENV2-US/BID-V594/2006 complex structure showing inter-E-dimer interactions
486 made by Fab light chain at 3f and 2f positions.

487

488

489 **Structural features of J9 and D14.F05.S03 Fab bound to spherical DENV strains**
490 **and its implications:**

491 The highest resolution, 3.85 Å cryo-EM structure of J9 Fab+DENV was
492 achieved in complex with the DENV2-US/BID-V594/2006 strain (Fig.1d,g, 2b). In case
493 of D14.F05.S03, structure determination to a global resolution of 4.5 Å was achieved
494 in complex with the DENV2-THSTI/TRC/01 strain (Fig.1f,i, 2d). Additionally, a 7.2 Å

495 cryo-EM structure of J9 Fab complexed with DENV2-THSTI/TRC/01 was also
496 determined, which showed clear density for the J9 Fab and identical binding features
497 as seen with the DENV2-US/BID-V594/2006 strain (Supplementary Fig.19). These
498 results demonstrate that the DENV2-THSTI/TRC/01 strain consists of homogenous
499 mature particles suitable for single-particle cryo-EM analyses. These results also
500 highlight that it is the binding of D14.F25.S02 Fab to DENV2 and not DENV2-strain
501 dependent properties which impeded higher resolution cryo-EM structure
502 determination of D14.F25.S02 Fab-bound DENV2-THSTI/TRC/01 sample.

503 In comparison to the D14.F25.S02 bound spherical DENV structures, the
504 occupancy of bound Fab was much higher in the case of D14.F05.S03 and J9.
505 D14.F05.S03 showed high occupancy of Fabs at its 3f and 2f positions (82%) with
506 relatively lower occupancy (50%) at the 5f positions (Fig.7a) (calculated as percentage
507 of the average map value of Fab/E-protein[28]). In case of J9, the fab bound equivalently
508 to the 5f and 3f positions (~60%) with lower occupancy at the 2f position (~35%)
509 (Fig.1d, Fig.7b). Analyses of fab interactions using the real-space refined atomic
510 models show that both D14.F05.S03 and J9 make minimal inter-E-dimer contacts. The
511 Fab light chains of both bnAbs making potential electrostatic interactions with Thr226
512 and Gln227 residues from an adjacent E-dimer within an E-raft (Fig.7a,b). However,
513 as in the case of D14.D25.S02, these intra-E-raft, inter-E-dimer contact residues are
514 not essential for Fab binding[16]. At the 5f position, the inter-E-dimer contacts change
515 for both J9 and D14.F05.S03. For D14.F05.S03, the orientation of the Fab atomic
516 model at 5f results in clashes with the atomic model of the E-protein from an adjacent
517 E-raft due to close juxtaposition of the protein chains (Fig.7a, Supplementary Table
518 6). These potential clashes of D14.F05.S03's light chain at the 5f position combined
519 with lack of inter-Fab stacking as seen at the 2f and 3f positions, could cause higher

520 variability in the Fab binding at the 5f vertices, which in turn may account for the lower
521 occupancy of D14.F05.S03 at 5f vertices as seen in the icosahedral-averaged cryo-
522 EM map (Fig.1f). For J9, the Fab light chain at 5f interacts with E-protein from an
523 adjacent E-dimer raft maintaining electrostatic interactions (Fig.7b). The lower J9
524 occupancy at 2f position could be due steric hindrance caused by J9 binding to
525 adjacent 5f and 3f positions in an E- raft (Fig.7b).

526

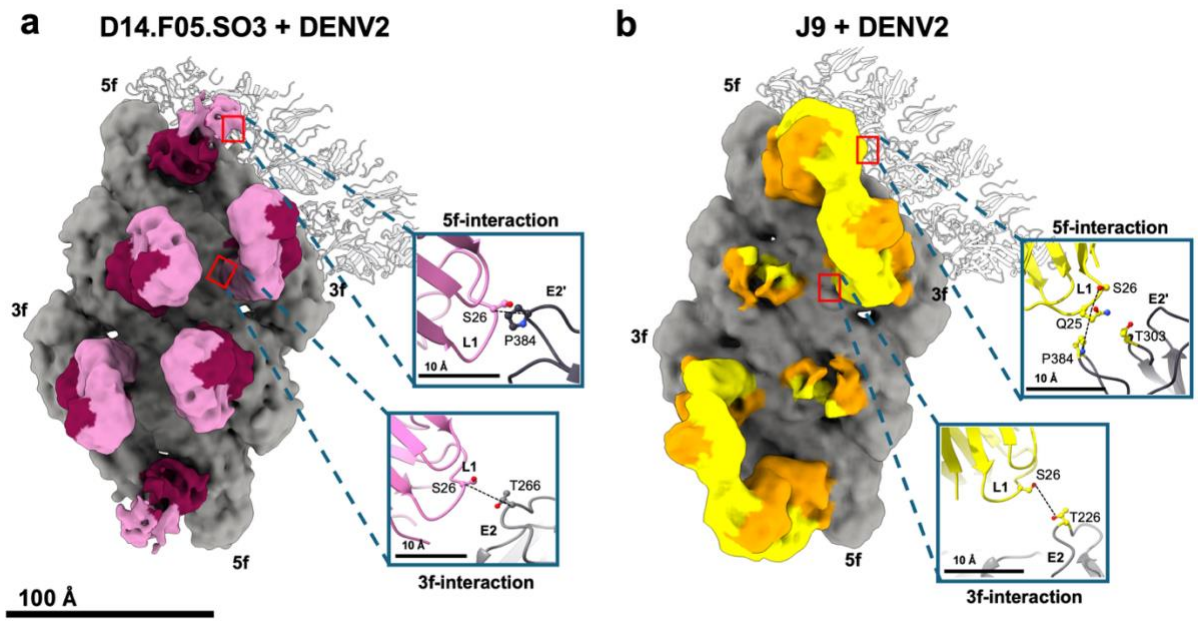

527

528 **Figure 7. D14.F05.S03 and J9 Fab arrangement on DENV E-raft**. **a.** Low threshold,
529 surface map rendering of D14.F05.S03 + DENV2-US/BID-V594/2006 map showing
530 higher Fab occupancy near 2-fold and 3-fold (3f) positions compared to the 5-fold (5f).
531 Based on the atomic models of the Fab and E-protein built into the electron density,
532 potential clashes seem likely between the Fab light chain (L1-S26) and E-protein (E2'-
533 P384) at the 5f position, with unrealistic inter-atomic distances of 2.01 Å between the
534 protein backbones. In contrast, at the 3f position, the closest distance between Fab
535 light chain (S26) and E-protein (E2-T266) is 7.51 Å. **b.** Low threshold, surface map

536 rendering of J9 + DENV2-US/BID-V594/2006 map showing higher Fab occupancy
537 near 5-fold (5f) and 3-fold (3f) positions compared to the 2-fold. Zoomed-in insets in
538 both panels show interaction of Fab light chain CDR1 (L1) with E-protein residues.
539 Based on the atomic model built in the electron density map, at the 5f position, the
540 closest distance between atoms in the J9 fab light chain (L1-S26) and E protein (E2'-
541 P384) from adjacent raft is 7.79 Å. At the 3f position, J9 fab light chain (L1 S26) residue
542 and E protein (T266) residue from adjacent raft is 8.86 Å. Residue contacts are
543 calculated as residues with distance between Ca-Ca backbone of Fab and E-protein
544 respectively.

545

546

547 **Discussion**:

548 HEDR bnAbs bind mature as well as tubular DENV as shown in this work
549 (Fig.8), along with incompletely mature virions as reported previously[16,18].
550 Expanded/bumpy DENV particles have been described to be present only at 37°C or
551 above [24,25] and all three bnAbs described here potently neutralize DENV at 37C[16,18].
552 The different DENV morphologies, ranging from spherical (mature, partially mature,
553 immature), to expanded and tubular virions, present varying quaternary surface
554 epitope arrangements and topology. Our current work along with previous reports[29]
555 shows that bnAb binding is differential to different DENV morphologies, suggesting
556 that these variation in DENV morphologies might serve as an adaptive mechanism for
557 escaping antibody-mediated neutralization and immune evasion by the virus. The
558 common surface feature across these virion forms is the presence of the E-dimer

559 configuration, which further emphasizes the importance of the E-dimer quaternary unit

560 as a critical antigenic target.

561

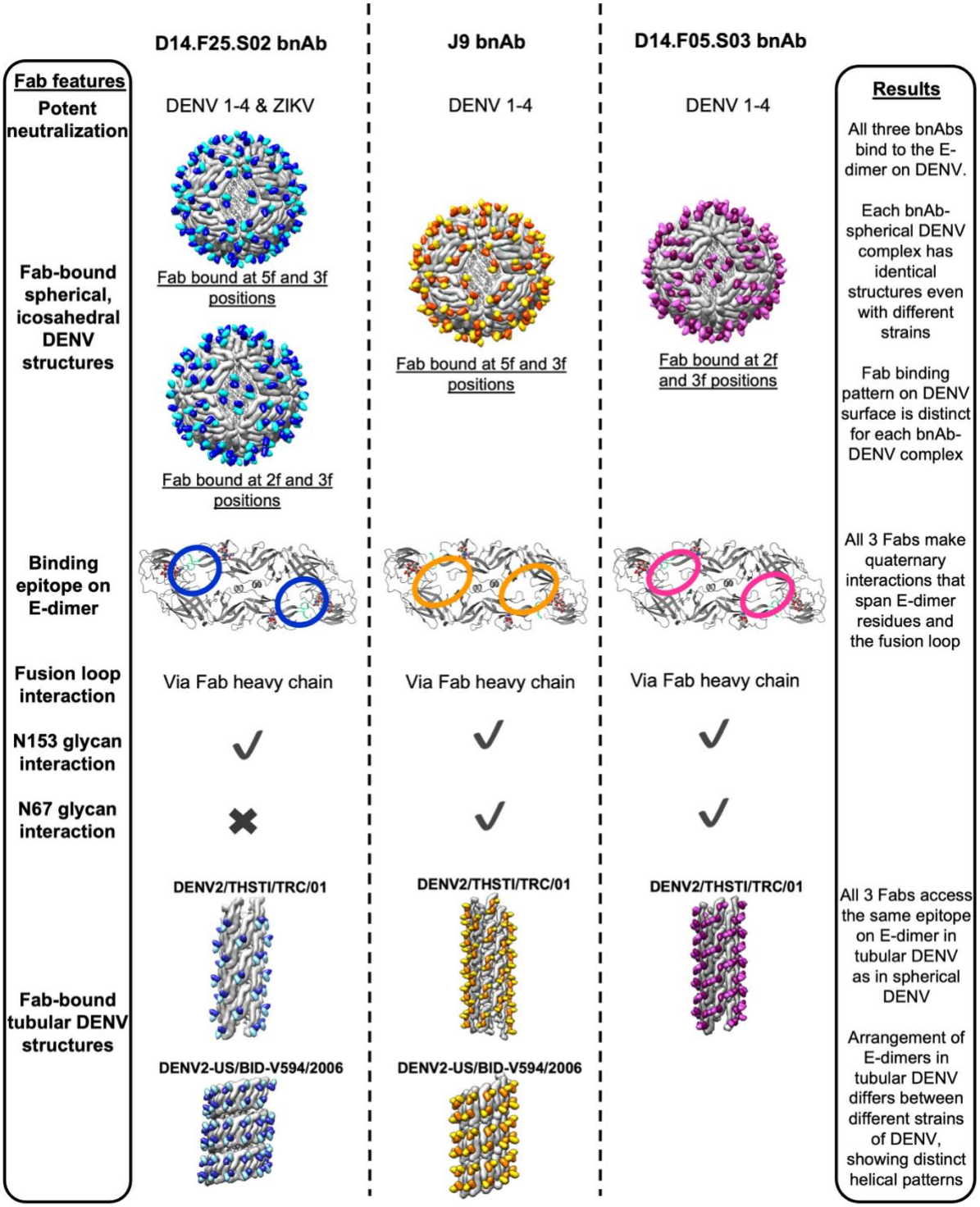

562

563 **Figure 8. Structural features of HEDR bnAb-bound DENV complexes and bnAb**

564 **binding epitopes.**

565

566 On comparing the five tubular DENV structures reported here, the helical
567 arrangements of E-dimers were similar within each DENV strain type, irrespective of
568 the Fab bound. The binding of an antibody, that locks the E-dimers together, seems
569 to be a prerequisite to form a globally regular arrangement of E-dimers on tubular
570 DENV, but the specific arrangement achieved by the E-dimers is influenced by the
571 virus strain type. In case of DENV2-US/BID-V594/2006 strain, the helical arrangement
572 resembles the E-raft sequentially wrapping around the tubular virion's length,
573 suggesting tighter inter-E-dimer and inter-E-raft interactions. However, in the
574 THSTI/TRC/01 strain, the relative strength of inter-E-dimer and E-raft interactions
575 appears to be weaker as the helical arrangement is drastically different from the
576 icosahedral E-raft arrangement.

577 The bnAb complex structures described here, show that these bnAbs directly
578 interact with the fusion loop on E-protein and occupy similar epitopes that bridge the
579 E-dimer, strongly suggesting that the bnAbs lock the E-dimers in the pre-fusion state.
580 The global bnAb footprints overlap with prM binding region on E-protein, which is
581 similar to that observed with EDE bnAbs[15,20], highlighting the conserved nature of this
582 epitope. Fusion loop exposure on the E-protein is necessary for attachment to
583 endosomal membranes and initiate viral membrane fusion in dengue virus cellular
584 entry[5,6]. Similarly, dissociation of E-dimers is necessary for conformational changes in
585 the E-proteins from pre-fusion to post-fusion structure, which has again been shown
586 to be essential for successful virus infection in cells[30,31]. Thus, the bnAbs likely inhibit
587 virus infection in cells by blocking exposure of the fusion loop and impeding E-dimer
588 dissociation, both steps that are essential for viral entry into host cells. Indeed,

589 previous report on the J9 bnAb has shown that the bnAb obstructs early entry steps in
590 virus infection[18], which further corroborates our results.

591 The heavy chain of the HEDR bnAbs interacts with the fusion loop and make
592 majority of the contacts within an E-dimer. The heavy chains of J9 and D4.F05.S03
593 are involved in interactions with both the conserved glycans and makes robust
594 contacts than the respective Fab's light chains. The light chain of the bnAbs is involved
595 in inter-E-dimer contacts both within and between E-rafts, likely stabilizing the bnAb
596 binding on the virions. As seen in case of D14.F25.S02, the inter-E-raft light chain
597 interactions are specific and necessary for neutralization activity of the bnAb.
598 However, the bnAbs also bind the tubular forms of DENV with good occupancy despite
599 the disruption in bnAb light-chain contacts as evident in the helical DENV2-
600 THSTI/TRC/01 complex structures. Thus, the bnAb heavy chain drives the overall
601 epitope recognition and potency of these HEDR antibodies.

602 From our results, it is evident that binding of HEDR category 1 bnAb,
603 D14.F25.S02, distorts spherical DENV. In case of the DENV2-THST/TRC/01 strain,
604 the effect of D14.F25.S02 binding at saturating concentrations had a dramatic effect
605 on virion structure and symmetry, impeding higher resolution structure determination
606 of the virion+Fab complex. However, the Fab binding did not destroy virion
607 organization but rather appears to have introduced significant local movements in the
608 E-proteins, as the virions' icosahedral symmetry was still discernible from the low-
609 resolution 3D density map. Remarkably, a 4.1 Å cryo-EM structure was achievable for
610 D14.F25.S02 to DENV2-US/BID-V594/2006 strain, indicating that this strain was
611 relatively resistant to distortion due to bnAb binding which could be a further reflection
612 of stronger interactions between the E-dimer and E-rafts in the US/BID-V594/2006

613 strain when compared to THSTI/TRC/01 strain. Nevertheless, analyses of 2D classes
614 and cryo-EM density maps show that binding of D14.F25.S02 to the US/BID-
615 V594/2006 virions does affect the topology of the E-protein surface, leading to many
616 virion particles being discarded during the 3D reconstruction process.

617 The major class of particles obtained from the D14.F25.S02+DENV2-US/BID-
618 V594/2006 dataset had the highest Fab occupancy at the icosahedral 5f position. The
619 local E-dimer arrangement at the 5f position likely facilitates D14.F25.S02 binding as
620 the larger gap between E-dimers surrounding the 5f vertices would allow easier
621 insertion of the bnAb HCDR3 loop between adjacent E-dimers. The bnAb also makes
622 inter-raft contacts that are unique to the 5f position which have been reported to be
623 crucial for its neutralization activity. These observations indicate that D14.F25.S02
624 binds preferentially to the 5f position on the icosahedral virus. However, the binding at
625 5f vertices effectively inhibits bnAb binding to the icosahedral 2f position, suggesting
626 that the bnAb binding at 5f causes local structural variations which limits bnAb binding
627 at the other sites. Notably, when D14.F25.S02 binds the 2f and 3f positions on the
628 virus, there is no binding observed at the 5f position, suggesting that once
629 D14.F25.S02 binds at 2f position, binding at 5f position is no longer possible for the
630 bnAb. These observations imply that binding of D14.F25.S02 at the 5f position causes
631 perturbations in the adjacent E-raft which impedes bnAb binding to the 2f position,
632 whereas binding of bnAb first to the 2f and 3f positions stabilizes the E-raft such that
633 E-dimer movement near the 5f position is restricted and thus, could inhibit bnAb
634 binding. Similar reports of local distortion to DENV structure have been reported for
635 EDE1 bnAb C10 which also strongly neutralizes DENV and ZIKV[28]. Binding of C10 to
636 purified DENV E-dimers has been shown to cause hinge-like motions in the E-
637 protein[15], along with preferred binding of bnAb to 5f and 3f positions and increased

638 dynamics of E-proteins with increasing Fab concentrations[28]. Thus, despite
639 differences in binding determinants and specific interactions to the E-proteins, HEDR
640 category-1 bnAbs and EDE1 bnAbs show similarities in disrupting E-protein
641 organization on spherical DENV surface.

642 HEDR category-2 bnAbs, J9 as well as D14.F05.S03, neutralize only DENV
643 and require interactions with the E-protein's conserved N153 glycan for their
644 neutralization activity. The HCDR3 loop of these bnAbs interacts with both the N153
645 glycan as well as the fusion loop on the E-protein. J9 and D14.F05.S03 also interact
646 with N67 glycan on E-protein which is not observed for D14.F25.S02, suggesting a
647 role for N67 glycan in epitope recognition. Notably, no distortion of the virion structure
648 is observed on binding with HEDR category-2 bnAbs.

649 Structural elucidation of these pan-DENV bnAb epitopes, as described here,
650 emphasizes the need for vaccine immunogen design that most closely imitate the E-
651 protein quaternary epitopes, including glycosylation, as presented on mature DENV
652 surface to elicit broad neutralization responses. For both, D14.F25.S02 and
653 D14.F05.S03, bivalent engagement as IgGs is necessary for potent neutralization
654 activity against DENV[16]. Based on the structural data obtained from D14.F25.S02 IgG
655 bound to DENV2 and previous published reports[13,32,33], it seems possible that virion
656 aggregation along with locking of E-dimers maybe essential for the neutralization
657 activity of these bnAbs. Despite the distortion caused by D14.F25.S02 binding to
658 DENV, the bnAb still has one of the highest reported neutralization potencies for a
659 pan-DENV and ZIKV bnAb[16]. When comparing neutralization of DENV serotypes
660 alone, J9 has one of the highest reported neutralization potencies reported till-date[18].
661 J9 has a relatively narrow footprint on the E-dimer surface, with most residues
662 important for its neutralization potency located near the fusion loop and the N153-

663 glycan loop. J9 also makes minimal inter-E-dimer and inter-E-raft contacts, with
664 primary determinants of bnAb binding localized to individual E-dimers. Furthermore,
665 J9 is capable of neutralizing DENV as IgG as well as Fab fragment. The potent activity
666 of J9 as Fab fragment increases its applicability as a therapeutic antibody while
667 avoiding any ADE effects caused by Fc regions present on IgGs. Similarly, despite the
668 need for bivalent engagement, antibody engineering[34,35] of D14.F25.S02 could be
669 leveraged for developing the bnAb as a pan-DENV+ZIKV therapeutic antibody. Thus,
670 engineered versions of these bnAbs may provide as much needed therapeutics
671 against severe dengue infections.

672

673

674

675 **Materials and Methods:**

676 Virus sample preparation:

677 Dengue virus serotype 2 strains THSTI/TRC/01 (GenBank: UNZ79673.1)_was
678 obtained as a kind gift from Dr. Guruprasad Medigishi, THSTI, Faridabad and US/BID-
679 V594/2006 (GenBank: ACA48992.1) was obtained through BEI Resources, NIAID,
680 NIH: Dengue Virus Type2, DENV-2/US/BID-V594/2006, NR-43280. Both virus strains
681 were propagated with minimal passages in mosquito cells (P-6) to 1L culture volumes
682 and purified in a similar manner as reported previously[2]. Mosquito cells (C6/36) were
683 cultured in Dulbecco's Modified Eagle Medium (DMEM) supplemented with 10% fetal
684 bovine serum (FBS) and 1% nonessential amino acids (NEAA). The cells were
685 maintained at 28°C with 5% CO2 in a 10-stack cell factory system (Nunc). Upon
686 reaching 70-75% confluency, cells were infected with DENV-2 using a multiplicity of

687 infection (MOI) of 0.1. The infection was allowed to proceed at 30°C with 5% CO2.
688 Post 2 hours of infection, the media was changed to complete media supplemented
689 with 5% FBS. At 20 hours post-infection, media was again changed to complete media
690 supplemented with 2% FBS. Supernatant medium containing the virus was collected
691 on 4th and 6th day post-infection. Virus-containing media was centrifuged at 9500xg
692 for 30 minutes and filtered through a 0.22-micron filter to remove all cell debris. The
693 filtrate was precipitated with 8% polyethylene glycol (PEG) overnight at 4°C, followed
694 by centrifugation at 9500xg for one hour to collect the PEG pellet. The pellet was then
695 resuspended in NTE buffer (120 mM NaCl, 20 mM Tris, 1 mM EDTA, pH 8.0). The
696 resuspended PEG pellet was sedimented through a 24% sucrose cushion. The
697 dissolved sucrose pellet applied to a potassium tartrate gradient (35%-10%) and
698 centrifugated at 32000 rpm for 2 hours at 4°C in a SW41-Ti swinging bucket rotor
699 (Beckman Coulter). Bands corresponding to the virus was extracted from the 20%
700 fraction of the discontinuous gradient, buffer exchanged and concentrated in NTE
701 buffer using a 100 kDa centrifugal filter. The purity and concentration of the virus
702 sample was estimated by visualising under negative staining transmission electron
703 microscopy (TEM) analysis.
704
705 Fab preparation:
706 Purified IgG of D14.F25.S02, J9, and D14.F05.S03 bnAbs were prepared as
707 previously reported[16,18]. BnAbs were digested with papain individually to generate Fab
708 fragments (~50kDa molecular weight) using a commercially available Fab
709 Fragmentation kit (G Biosciences) (Cat. # 786-273). Fabs were then separated in
710 flowthrough by passing over a Protein-A column. Concentrations of Fabs obtained for

711 F25.S02, J9, and F05.S03 were 0.9 mg/ml, 0.6 mg/ml and 1.01 mg/ml, respectively.
712 Concentration of F25.S02 IgG sample was 1mg/ml.
713
714 Cryo-EM sample preparation:
715 Purified DENV samples at an approximate concentration of 0.25 mg/ml (E-
716 glycoprotein concentration) were incubated with the respective Fabs and F25.S02
717 IgG at room temperature for 45 minutes. In case of D14.F25.S02, molar ratio of Fab
718 to virus was 4:1 and molar ratio of IgG to virus was 1:1. For J9 and D14.F05.S03,
719 molar ratio of Fab to virus was maintained at 2:1 and 2.5:1 respectively. For
720 estimating the concentration of dengue virus needed for the experiments, the
721 concentration of E-glycoprotein estimated from SDS-PAGE was used. Ultra-thin
722 lacey carbon grids (300 or 400 mesh) were glow discharged using 25 mA current for
723 30s with a PELCO EasiGlow machine. Aliquots of 3ul virus-Ab mixture were applied
724 on glow discharged grids and plunge-frozen with FEI Vitrobot mark IV for DENV-2-
725 THST1/TRC/01 + Fab complexes (Blot time – 8s, Temperature - 4° C, Humidity –
726 100%) and Leica EM GP2 for DENV2-US/BID-V594/2006 + Ab complexes (Blot time
727 – 3.5s, Temperature - 4° C, Humidity – 100%).
728
729 Cryo-EM data collection:
730 All DENV-2-THST1/TRC/01 and Fab complex samples were imaged in Talos Arctica
731 (FEI, ThermoFisher Inc.), operating at 200 keV, with a K2 summit electron detector
732 (Gatan Inc.). Micrographs were collected with a pixel size of 1.16 Å/pixel, at a total
733 dose of 38 - 40 $e^-/Å^2$ fractionated into 20 frames per image, and with defocus range of
734 -1.5 to -2.5 μm.

735 DENV2 US/BID-V594/2006 samples complexed with J9 Fab, F25.S02 Fab and IgG
736 were imaged using Titan Krios G3I, operating at 300 keV with a K3 detector and an
737 energy filter (Bioquantum imaging) operating at a slit width 20eV. Micrographs for each
738 dataset were collected with a total dose of 40 – 42 $e^-/Å^2$ fractionated into 38 frames
739 per image at a defocus range of -1 µm to -2.5µm and with a pixel size of 1.1 Å/pixel.
740
741 Cryo-EM data processing:
742 A combination of RELION-4.0[36] and cryoSPARC version 4.7.0 software package[37]
743 was used for data processing following standard single particle analysis (SPA) steps.
744 Frame alignment was carried out using Relion's own implementation of motion
745 correction or Cryosparc's Patch motion correction. CTF estimation was performed
746 using CTFFIND4[38].
747 D14.F25.S02-virus complex datasets: For the D14.F25.S02 Fab + DENV2 US/BID-
748 V594/2006 complex, 7405 micrographs were collected at a magnification of 81000x
749 with corresponding pixel size of 1.1Å/Pixel. Dataset of D14.F25.S02 IgG + DENV2
750 US/BID-V594/2006 was also collected at the same magnification and microscope
751 settings as the Fab datasets with a total of 4172 images. Virion particles were manually
752 picked from both datasets, with 22000 particles picked from the Fab dataset and 8176
753 particles from the IgG dataset. Subsequent rounds of 2D classification and 3D
754 classification were performed on the individual particle datasets. For the Fab complex,
755 a 3D class with 2305 particles was selected and used for non-uniform refinement[39]
756 and CTF refinement[40] which resulted in a 4.09 Å density map showing Fab density
757 near 5f and 3f symmetry vertices. A smaller 3D class containing 905 particles was
758 selected for non-uniform refinement which resulted in an 8.45 Å density map of the
759 Fab bound near the 2f-3f symmetry vertices. For the IgG dataset, 2D classification, 3D

760 refinement and post-processing was carried out in RELION-4.0. The final 3D
761 reconstruction of 7.65 Å global resolution was calculated from 1045 particles selected
762 from 3D classification.
763 For the D14.F25.S02 Fab + DENV-2-THST1/TRC/01 complex, 4000 micrographs
764 were collected at a magnification of 36000x with corresponding pixel size of
765 1.16Å/Pixel. From these images, 26782 particles were manually picked and subjected
766 to unsupervised 2D classification in RELION-4.0. The best classes which showed
767 apparent Fab densities were selected for reference-based 3D classification in
768 RELION-4.0. Different starting models, including a sphere, mature DENV structure
769 and the determined DENV2-US/BID/V594/2006+D14.F25.S02 Fab structure were
770 used for 3D classification. All the classification routines resulted in similar results.
771 Finally, a total of 4715 particles from the best classes of 3D classification from
772 RELION4 were utilised for 3D non-uniform refinement in cryoSPARC-4.7.0 to generate
773 a 3D density map at 19 Å global resolution.
774
775 J9-virus complex datasets: A total of 4756 micrographs were collected for the J9 +
776 DENV2 US/BID-V594/2006 complex at a magnification of 81000x with corresponding
777 pixel size of 1.1Å/Pixel. Around 15000 particles were manually picked in RELION-4.0.
778 Further, the particle coordinates were imported to cryoSPARC-4.7.0. After 2D and 3D
779 classification, 2900 best particles were used for iterative non-uniform refinement and
780 CTF refinement, resulting in an electron density map of 3.85 Å global resolution.
781 For the J9 + DENV-2-THST1/TRC/01 complex, 1100 images were collected at a
782 magnification of 36000x with corresponding pixel size of 1.16Å/Pixel. Of the 10108
783 manually picked particles, only 668 particles showed clear Fab densities after 2D
784 classification in RELION-4.0. These particles were then used non-uniform refinement

785 in cryoSPARC-4.7.0. The 3D refinement resulted in an electron density map of 7.21 Å
786 global resolution.
787
788 D14.F05.S03-virus complex datasets: A total of 3176 micrographs were collected at a
789 magnification of 36000x with corresponding pixel size of 1.16Å/pixel for D14.F05.S03
790 + DENV-2-THST1/TRC/01 complex. From these images, 32650 particles were
791 manually picked using RELION-4.0 software. The manually picked particle
792 coordinates were further imported to cryoSPARC-4.7.0 for further processing. A final
793 set of 4299 particles were selected for 3D refinement following non-reference 2D
794 classification and reference-based 3D classification. Subsequent iterative non-uniform
795 refinement and CTF refinement resulted in a 3D density map with global resolution of
796 4.51 Å.
797
798 Real space refinement and model fitting in icosahedral maps:
799 The complete IgG sequence of D14.F25.S02 and the Fab portion sequence of
800 D14.F25.S02, J9, and D14.F05.S03 were used to generate atomic models in
801 AlphaFold3 web server[41]. The sequences of DENV-2-THST1/TRC/01 and DENV2-
802 US/BID-V594/2006 were used as queries for homology modelling in the SWISS-
803 MODEL web server[42] using mature DENV-2 structures (PDB IDs:7KV8 and 7V3F) as
804 a template. The asymmetric unit of the virus and Fab models were initially rigid body
805 fitted separately in respective maps. For the different high-resolution maps, different
806 approaches were used for map sharpening. For D14.F25.S02 and D14.F05.S03
807 maps, map sharpening was done using the Phenix software package[43]. In case of the
808 J9 map, map sharpening was carried out using DeepEMhancer[44]. Further, the
809 generated atomic models were real-space refined using the Phenix software[45,46].

810 Geometry restraints and Ramachandran clashes were adjusted as needed using
811 COOT[47]. Glycan components were added to the E-protein atomic models using higher
812 resolution E-protein structures (PDB IDs: 4UT6, 4UTA) as reference. Glycan residues
813 (N-acetyl glucosamine (NAG), α-D-mannopyranose (MAN) and β-D-mannopyranose
814 (BMA)) were manually added to N67 and N153 residues of the E protein using COOT
815 according to the map densities and were included in the atomic models for real-space
816 refinement.
817 For the highest resolution J9 Fab-virus complex map, the model used for real-space
818 refinement included the complete asymmetric unit containing three E-protein
819 monomers and Fabs at 5f and 3f position. For the highest resolution D14.F25.S02
820 Fab-virus complex map, model used for real-space refinement included the E-dimer
821 with Fab at 5f position. For the highest resolution D14.F05.S03 Fab-virus complex
822 map, model used for real-space refinement included the complete asymmetric unit
823 containing 3 E-protein monomers and Fabs at 3f position. Maps and models were
824 analysed and figures prepared using UCSF Chimera[48] and UCSF ChimeraX[49].
825
826 <u>Localized reconstruction at sub-icosahedral symmetry positions:</u>
827 Particles from the initial 3D classification of icosahedral reconstruction were imported
828 to SCIPION-3[50]. Vector coordinates of 5 and 3fold vertices were applied and the sub-
829 particles were defined[51]. The defined sub-particles were extracted, and 3D
830 classification and refinement were performed in RELION-4.0 according to standard
831 procedures. Circular masks which covered the Fabs and half of the E-dimer length at
832 a given vertex, were applied during classification and initial refinement steps.
833 The localized reconstruction from 5-fold and 3-fold symmetry positions of the J9 +
834 DENV2/US/HBID-V594/2006 complex was performed with an initial set of 42886 and

835 71487 defined and filtered sub-particles, respectively. After classification, 20077 and
836 26545 best-aligned sub-particles were used for 3D refinement resulting in 4.55 Å (5-
837 fold) and 4.4 Å (3-fold) resolution maps. For the D14.F05.S03 + DENV-2
838 THSTI/TRC/01 complex, localized reconstruction for the 3f vertices was performed
839 with 193844 defined sub-particles. After 3D classification, 75433 sub-particles were
840 used in the final refinement to produce a map of 4.84 Å global resolution. In case of
841 D14.F25.S02, 3D classification of sub-particles extracted at 5-fold and 3-fold positions
842 failed to give any class that showed clear Fab densities and thus were not refined
843 further. The 3D density maps were sharpened in DeepEMhancer[44]. Glycans where
844 manually added to improved density regions using COOT[47] based on higher resolution
845 E-protein structures (PDB IDs: 4UT6 and 4UTA) as references. The atomic models
846 were fitted as rigid bodies using UCSF Chimera[48] followed by real-space refined in
847 Phenix[45].
848
849 Difference map calculations:
850 The atomic models of each E-dimer + Fab complex were aligned using the E-dimer as
851 reference in UCSF Chimera. Next, the atomic models of the three Fabs, J9,
852 D14.F25.S02, and D14.F05.S03, from the complex structures were used to generate
853 volumes in UCSF Chimera, maintaining equal grid spacing and scaling. The difference
854 between each pair of Fab volumes was calculated using the RELION-4.0 command
855 interface (relion_image_handler). The computed difference volumes show the
856 common footprint shared between Fabs, which lies over the E-protein's fusion loop
857 region.
858
859

860 Helical reconstructions of tubular DENV regions:

861 For the helical reconstruction of tubular regions from DENV2 US/BID-V594/2006
862 virions, helical segments were manually picked in segment picking of RELION-4.0. For
863 both D14.F25.S02- and J9-bound virions, the initial helical rise and twist for DENV2
864 US/BID-V594/2006 tubular particles were estimated manually in UCSF Chimera by
865 arranging the Fab+E-dimer models around a cylinder of same dimensions as the virion
866 segments with minimal clashes. A 2D projection of the manually arranged helical
867 geometries was then used to match with the arrangement observed in 2D class
868 averages of tubular particles with no symmetry applied. An initial rise and twist for
869 D14.F25.S02-bound segments (rise=10 Å and twist-=30°) and for J9-bound segments
870 (rise=13Å and twist=36°) was used for reference-free helical 2D classification[52] in
871 RELION-4.0. Best 2D classes containing a total of 2188 segments for D14.F25.S02-
872 bound dataset and 1361 segments for J9-bound dataset were subjected to 3D
873 classification with initial estimates using a 3D-cylinder as starting model. In case of
874 D14.F25.SO2 dataset, 405 segments were imported for final helical 3D reconstruction
875 in cryoSPARC-4.7.0 using non-uniform refinement option with rise and twist of 11.25Å
876 and 29.48° which yielded a density map of global resolution 14.7 Å. For the J9 dataset,
877 a best class with 253 segments was used for helical 3D reconstruction in RELION-4.0
878 with rise and twist of 12.83Å and 35.83° that resulted in a 3D map with estimated global
879 resolution of 44Å.

880

881 For bnAb bound tubular-shaped particles found in DENV-2 THSTI/TRC/01 datasets,
882 the tubular-shaped regions of the virions were manually picked following the helical
883 particle picking protocol of RELION-4.0 and unsupervised 2D classification was
884 performed. Class averages with distinct Fourier amplitude patterns were imported to

885 PyHi Fourier Bessel indexing software[53] and helical rise and twist values were
886 calculated for the antibody-virus complexes. From the calculated rise and twist,
887 another round of unsupervised helical 2D classification was performed, and the
888 particles were extracted with the same parameters for reference-based 3D
889 classification. For initial 3D classifications 3D-cylinder was used as startup model. The
890 best 3D classes were selected, and the particle co-ordinates were transferred to
891 cryoSPARC-4.7.0 for final helical reconstruction using non-uniform refinement option.
892 For the J9 + DENV-2 THSTI/TRC/01 complex, 19792 segments were manually
893 picked, and after classification routines, 5769 segments were used for the final 3D
894 refinement, which resulted in a helical density map of 14.41 Å. Similarly, for the
895 D14.F25.S02 and D14.F05.S03 complexes, 8264 and 8045 segments were
896 respectively picked in manual mode, and final sets of 1355 (for D14.F25.S02) and
897 1311 segments (for D14.F05.S03) were used to generate 3D maps at global
898 resolutions of 17.37 Å and 17.29 Å respectively.
899 In all helical reconstructions, a hollow cylindrical mask was used which focused on the
900 E-protein and membrane layer of DENV tubular particles during all the refinement
901 steps.
902
903 <u>Inner volume calculations for capsule-shaped DENV2-US/BID-V4594/2006:</u>
904 For D14.F25.S02-bound virions:
905 Average length of cylindrical portion in capsule-shaped DENV = 79 nm
906 Inner radius of capsule = 5.5 nm.
907 Thus, internal volume of cylindrical portion in capsule-shaped DENV = 7.503 x 10^-24
908 m^3
909 Assuming, volume of one copy of viral genome[26,54] = 3.8 x 10-24 m^3

910 Number of genome copies that can be possibly accommodated in capsule-shaped
911 DENV = 1.9
912
913 For J9-bound virions:
914 Average length of cylindrical portion in capsule-shaped DENV = 74.149nm
915 Inner radius of capsule= 6nm
916 Thus, internal volume of cylindrical portion of capsule-shaped DENV = 8.38 x 10^ $^{-24}$
917 m3
918 Assuming, volume of one copy of viral genome[26,54] = 3.8 x 10-24 m^3
919 Number of genome copies that can be possibly accommodated in capsule-shaped
920 DENV = 2.2
921

922 **References**:

923 1. Bhatt, S. *et al.* The global distribution and burden of dengue. *Nature* **496**, 504–507
924 (2013).
925 2. Kuhn, R. J. *et al.* Structure of Dengue Virus. *Cell* **108**, 717–725 (2002).
926 3. Modis, Y., Ogata, S., Clements, D. & Harrison, S. C. A ligand-binding pocket in the
927 dengue virus envelope glycoprotein. *Proceedings of the National Academy of*
928 *Sciences* **100**, 6986–6991 (2003).
929 4. Zhao, R. *et al.* Flavivirus: From Structure to Therapeutics Development. *Life* **11**, 615
930 (2021).
931 5. Huang, C. Y.-H. *et al.* The dengue virus type 2 envelope protein fusion peptide is
932 essential for membrane fusion. *Virology* **396**, 305–315 (2010).
933 6. Nicholls, C. M. R., Sevvana, M. & Kuhn, R. J. Structure-guided paradigm shifts in
934 flavivirus assembly and maturation mechanisms. in 33–83 (2020).
935 doi:10.1016/bs.aivir.2020.08.003.
936 7. Chong, L. C. & Khan, A. M. Identification of highly conserved, serotype-specific
937 dengue virus sequences: implications for vaccine design. *BMC Genomics* **20**, 921
938 (2019).
939 8. Dejnirattisai, W. *et al.* Cross-Reacting Antibodies Enhance Dengue Virus Infection in
940 Humans. *Science (1979)* **328**, 745–748 (2010).
941 9. Rey, F. A., Stiasny, K., Vaney, M.-C., Dellarole, M. & Heinz, F. X. The bright and the
942 dark side of human antibody responses to flaviviruses: lessons for vaccine design.
943 *EMBO Rep* **19**, 206–224 (2018).

944 10. Morrone, S. R. & Lok, S.-M. Structural perspectives of antibody-dependent
945 enhancement of infection of dengue virus. *Curr Opin Virol* **36**, 1–8 (2019).
946 11. Katzelnick, L. C. *et al.* Antibody-dependent enhancement of severe dengue disease in
947 humans. *Science* **358**, 929–932 (2017).
948 12. Pierson, T. C. & Diamond, M. S. The continued threat of emerging flaviviruses. *Nat*
949 *Microbiol* **5**, 796–812 (2020).
950 13. Zhang, S. *et al.* A Human Antibody Neutralizes Different Flaviviruses by Using
951 Different Mechanisms. *Cell Rep* **31**, 107584 (2020).
952 14. Dejnirattisai, W. *et al.* Dengue virus sero-cross-reactivity drives antibody-dependent
953 enhancement of infection with zika virus. *Nat Immunol* **17**, 1102–1108 (2016).
954 15. Sharma, A. *et al.* The epitope arrangement on flavivirus particles contributes to Mab
955 C10's extraordinary neutralization breadth across Zika and dengue viruses. *Cell* **184**,
956 6052-6066.e18 (2021).
957 16. Lubow, J. *et al.* Single B cell transcriptomics identifies multiple isotypes of broadly
958 neutralizing antibodies against flaviviruses. *PLoS Pathog* **19**, e1011722 (2023).
959 17. Barba-Spaeth, G. *et al.* Structural basis of potent Zika–dengue virus antibody cross-
960 neutralization. *Nature* **536**, 48–53 (2016).
961 18. Durham, N. D. *et al.* Broadly neutralizing human antibodies against dengue virus
962 identified by single B cell transcriptomics. *Elife* **8**, (2019).
963 19. Dejnirattisai, W. *et al.* A new class of highly potent, broadly neutralizing antibodies
964 isolated from viremic patients infected with dengue virus. *Nat Immunol* **16**, 170–177
965 (2015).
966 20. Rouvinski, A. *et al.* Recognition determinants of broadly neutralizing human
967 antibodies against dengue viruses. *Nature* **520**, 109–113 (2015).
968 21. Rey, F. A., Stiasny, K., Vaney, M.-C., Dellarole, M. & Heinz, F. X. The bright and the
969 dark side of human antibody responses to flaviviruses: lessons for vaccine design.
970 *EMBO Rep* **19**, 206–224 (2018).
971 22. Plevka, P. *et al.* Maturation of flaviviruses starts from one or more icosahedrally
972 independent nucleation centres. *EMBO Rep* **12**, 602–606 (2011).
973 23. Junjhon, J. *et al.* Influence of pr-M Cleavage on the Heterogeneity of Extracellular
974 Dengue Virus Particles. *J Virol* **84**, 8353–8358 (2010).
975 24. Zhang, X. *et al.* Dengue structure differs at the temperatures of its human and
976 mosquito hosts. *Proc Natl Acad Sci U S A* **110**, 6795–9 (2013).
977 25. Fibriansah, G. *et al.* Structural changes in dengue virus when exposed to a
978 temperature of 37°C. *J Virol* **87**, 7585–92 (2013).
979 26. Morrone, S. R. *et al.* High flavivirus structural plasticity demonstrated by a non-
980 spherical morphological variant. *Nat Commun* **11**, 3112 (2020).
981 27. Kudlacek, S. T. *et al.* Designed, highly expressing, thermostable dengue virus 2
982 envelope protein dimers elicit quaternary epitope antibodies. *Sci Adv* **7**, eabg4084
983 (2021).
984 28. Lim, X.-X. *et al.* Human antibody C10 neutralizes by diminishing Zika but enhancing
985 dengue virus dynamics. *Cell* **184**, 6067-6080.e13 (2021).
986 29. Fibriansah, G., Lim, X.-N. & Lok, S.-M. Morphological Diversity and Dynamics of
987 Dengue Virus Affecting Antigenicity. *Viruses* **13**, 1446 (2021).
988 30. Chao, L. H. *et al.* How small-molecule inhibitors of dengue-virus infection interfere
989 with viral membrane fusion. *Elife* **7**, (2018).
990 31. Stiasny, K., Fritz, R., Pangerl, K. & Heinz, F. X. Molecular mechanisms of flavivirus
991 membrane fusion. *Amino Acids* **41**, 1159–1163 (2011).

992 32. Zhou, Q. F. *et al.* Structural basis of Chikungunya virus inhibition by monoclonal
993 antibodies. *Proceedings of the National Academy of Sciences* **117**, 27637–27645
994 (2020).
995 33. Wang, J. *et al.* A Human Bi-specific Antibody against Zika Virus with High Therapeutic
996 Potential. *Cell* **171**, 229-241.e15 (2017).
997 34. Hale, G. Living in LALA land? Forty years of attenuating Fc effector functions.
998 *Immunol Rev* **328**, 422–437 (2024).
999 35. Rosenstein, S. *et al.* Production of F(ab')2 from Monoclonal and Polyclonal
1000 Antibodies. *Curr Protoc Mol Biol* **131**, e119 (2020).
1001 36. Kimanius, D., Dong, L., Sharov, G., Nakane, T. & Scheres, S. H. W. New tools for
1002 automated cryo-EM single-particle analysis in RELION-4.0. *Biochem J* **478**, 4169–
1003 4185 (2021).
1004 37. Punjani, A., Rubinstein, J. L., Fleet, D. J. & Brubaker, M. A. cryoSPARC: algorithms
1005 for rapid unsupervised cryo-EM structure determination. *Nat Methods* **14**, 290–296
1006 (2017).
1007 38. Rohou, A. & Grigorieff, N. CTFFIND4: Fast and accurate defocus estimation from
1008 electron micrographs. *J Struct Biol* **192**, 216–21 (2015).
1009 39. Punjani, A., Zhang, H. & Fleet, D. J. Non-uniform refinement: adaptive regularization
1010 improves single-particle cryo-EM reconstruction. *Nat Methods* **17**, 1214–1221 (2020).
1011 40. Zivanov, J., Nakane, T. & Scheres, S. H. W. Estimation of high-order aberrations and
1012 anisotropic magnification from cryo-EM data sets in RELION-3.1. *IUCrJ* **7**, 253–267
1013 (2020).
1014 41. Abramson, J. *et al.* Addendum: Accurate structure prediction of biomolecular
1015 interactions with AlphaFold 3. *Nature* **636**, E4 (2024).
1016 42. Waterhouse, A. *et al.* SWISS-MODEL: homology modelling of protein structures and
1017 complexes. *Nucleic Acids Res* **46**, W296–W303 (2018).
1018 43. Terwilliger, T. C., Sobolev, O. V, Afonine, P. V & Adams, P. D. Automated map
1019 sharpening by maximization of detail and connectivity. *Acta Crystallogr D Struct Biol*
1020 **74**, 545–559 (2018).
1021 44. Sanchez-Garcia, R. *et al.* DeepEMhancer: a deep learning solution for cryo-EM
1022 volume post-processing. *Commun Biol* **4**, 874 (2021).
1023 45. Afonine, P. V *et al.* Real-space refinement in PHENIX for cryo-EM and
1024 crystallography. *Acta Crystallogr D Struct Biol* **74**, 531–544 (2018).
1025 46. Liebschner, D. *et al.* Macromolecular structure determination using X-rays, neutrons
1026 and electrons: recent developments in Phenix. *Acta Crystallogr D Struct Biol* **75**, 861–
1027 877 (2019).
1028 47. Emsley, P., Lohkamp, B., Scott, W. G. & Cowtan, K. Features and development of
1029 Coot. *Acta Crystallogr D Biol Crystallogr* **66**, 486–501 (2010).
1030 48. Pettersen, E. F. *et al.* UCSF Chimera--a visualization system for exploratory research
1031 and analysis. *J Comput Chem* **25**, 1605–12 (2004).
1032 49. Meng, E. C. *et al.* UCSF ChimeraX: Tools for structure building and analysis. *Protein*
1033 *Sci* **32**, e4792 (2023).
1034 50. de la Rosa-Trevín, J. M. *et al.* Scipion: A software framework toward integration,
1035 reproducibility and validation in 3D electron microscopy. *J Struct Biol* **195**, 93–9
1036 (2016).
1037 51. Ilca, S. L. *et al.* Localized reconstruction of subunits from electron cryomicroscopy
1038 images of macromolecular complexes. *Nat Commun* **6**, 8843 (2015).

1039 52. He, S. & Scheres, S. H. W. Helical reconstruction in RELION. *J Struct Biol* **198**, 163–
1040 176 (2017).
1041 53. Zhang, X. Python-based Helix Indexer: A graphical user interface program for finding
1042 symmetry of helical assembly through Fourier-Bessel indexing of electron microscopic
1043 data. *Protein Sci* **31**, 107–117 (2022).
1044 54. Yoffe, A. M. *et al.* Predicting the sizes of large RNA molecules. *Proc Natl Acad Sci U*
1045 *S A* **105**, 16153–8 (2008).

1046

1047

1048 **Data availability**

1049 Cryo-electron microscopy density maps and corresponding atomic models presented
1050 in this study has been submitted to the Electron Microscopy Data Bank (EMDB) and
1051 RCSB Protein Data Bank (PDB). Accession codes for the same are as follows:

S.no.	Sample description	EMDB ID	PDB ID
1.	J9 Fab + DENV2-US/BID-V594/2006 icosahedral reconstruction	EMD-63759	9MAV
2.	5-fold Localized reconstruction of J9 Fab + DENV2-US/BID-V594/2006 icosahedral reconstruction	EMD-63760	9MAX
3.	3-fold Localized reconstruction of J9 Fab + DENV2-US/BID-V594/2006 icosahedral reconstruction	EMD-63761	9MAY
4.	J9 Fab + DENV2-US/BID-V594/2006 helical reconstruction	EMD-63762	9MAZ
5.	J9 Fab + DENV2-THSTI/TRC/01 icosahedral reconstruction	EMD-63763	9MB0
6.	J9 Fab + DENV2-THSTI/TRC/01 helical reconstruction	EMD-63764	9MB1

7.	D14.F25.S02 Fab + DENV2-US/BID-V594/2006 icosahedral reconstruction (5f-3f map)	EMD-63643	9M5H, 9U33
8.	D14.F25.S02 Fab + DENV2-US/BID-V594/2006 icosahedral reconstruction (2f-3f map)	EMD-63813	9U38
9.	D14.F25.S02 IgG + DENV2-US/BID-V594/2006 icosahedral reconstruction	EMD-63812	9U37
10.	D14.F25.S02 Fab + DENV2-US/BID-V594/2006 helical reconstruction	EMD-63809	9U34
11.	D14.F25.S02 Fab + DENV2-THSTI/TRC/01 helical reconstruction	EMD-63810	9U35
12.	D14.F25.S02 Fab + DENV2-THSTI/TRC/01 icosahedral reconstruction	EMD-63811	9U36
13.	D14.F05.S03 Fab + DENV2-THSTI/TRC/01 icosahedral reconstruction	EMD-63801	9MCF
14.	3-fold Localized reconstruction of D14.F05.S03 Fab + DENV2-THSTI/TRC/01 icosahedral reconstruction	EMD-63800	9MCE
15.	D14.F05.S03 Fab + DENV2-THSTI/TRC/01 helical reconstruction	EMD-63815	9U3J

Competing interests

The authors declare no competing interests.

Supplementary Information:

Supplementary figures and tables including extended data information are included in separate supplementary information document.

Acknowledgements

We thank the Advanced Center for Cryo-Electron Microscopy (ACCEM) facility at Indian Institute of Science, Bangalore (IISc) and the DST-SATHI Cryo-EM facility at IIT-Delhi for data collection time and support. We also thank the Bioimaging facility at IISc which houses the 120kV room temperature TEM for time and support. We thank Dr. Kelly Lee, University of Washington for his support during project initiation and scientific discussions. This study was supported by SERB Power grant (SPG/2021/002433) to V.M.P. This study was also partially supported through the India Alliance DBT Wellcome Intermediate fellowship (IA/I/22/1/506233) and start-up grant fund (IISc) to V.M.P; IoE fellowship to S.S and A.R, and Prime Minister's Research Fellowship (PMRF), Govt. of India, to A.C.

Author contributions:

Conceptualization L.G and V.M.P; IgG purification, J.L; virus purification, A.C and S.C; Fab production, virus-complex preparations, cryo-EM data collection and data processing, A.R, A.C and S.S; EM data analysis, A.C, A.R, S.S and V.M.P; Writing, V.M.P, A.C, A.R and S.S; resources, V.M.P.; funding acquisition, V.M.P.